

Abstract

ERVIN, JENNIFER KELLY. Post Heat Treatment Effects of Ti-6Al-4V Produced via Solid Freeform Electron Beam Melting. (Under the direction of Professor Jerome J. Cuomo).

Traditionally, Ti-6Al-4V components are fabricated by forging or casting. However, these methods of production require expensive dies or molds. The cost per part is very high for those parts produced in low quantities. The solid freeform electron beam melting process aims to produce high dimensional tolerance parts with similar mechanical properties at a lower cost by melting Ti-6Al-4V powder in a layer by layer fashion using high energy electrons. Due to the directional solidification effects, the microstructure seen in this process consists of a columnar grain structure along the growth direction and an equiaxed structure at the cross-sectional growth plane. This type of structure is thought to contribute to the anisotropy of tensile properties discovered in previous research. Although, preferred orientation of the α laths may play a role as well. Heat treatments above the β transus are performed in order to improve the tensile properties, specifically ductility, with intentions to remove preferred orientation and to disunite the columnar grain structure. Tensile testing, fractography, optical microscopy, and x-ray diffraction are used to characterize and compare the as-processed and β heat treated electron beam melted specimens. It is found for all β treated conditions, the ductility increases compared to the as-processed specimens, although the strength decreases. The mode of fracture changes from ductile dimple rupture in the as-processed condition to transgranular cleavage with ductile dimple rupture for the heat treated specimens. The macrostructure and microstructure in the as-processed and heat treated specimens contrasted greatly. The macrostructure changes from a fully columnar structure to a mixture of columnar and equiaxed grains. A fine acicular microstructure is observed in the as-processed samples, whereas a broad lamellar colony microstructure is formed during heat

treatment. The presence of a colony microstructure is a possible reason for the improvement in ductility. From the x-ray data obtained, the preferred orientation is not reduced but instead increases after heat treating in the β region which likely is a result of the favorable rearrangement of slip systems due to the change in α lath orientation.

Post Heat Treatment Effects of Ti-6Al-4V Produced via Solid Freeform Electron Beam Melting

by
Jennifer K. Ervin

A thesis submitted to the graduate faculty of
North Carolina State University
in partial fulfillment of the
requirements of the degree of
Master of Science

Materials Science and Engineering

Raleigh, North Carolina

2008

APPROVED BY:

Dr. Denis R. Cormier

Dr. Korukonda L. Murty

Dr. Jerome J. Cuomo
Chair of Advisory Committee

Biography

Jennifer Kelly Ervin was born on August 15, 1982 in Kinston, North Carolina. She received her bachelor's degree in Materials Science and Engineering from North Carolina State University in 2005. After graduation, Kelly traveled to Rajamangala University of Technology in Trang, Thailand where she volunteered as a teaching assistant. She returned to the department to obtain her master of science with an emphasis in physical metallurgy under the direction of Dr. Jerome J. Cuomo.

Acknowledgements

I would like to thank Dr. Jerome J. Cuomo for his guidance and support throughout my years as an undergraduate and graduate student. The ample “opportunities” which he has presented to me are invaluable. I would also like to thank the members of my committee Dr. Denis R. Cormier and Dr. Korukonda L. Murty. A special thank you goes to Dr. Ray B. Benson, Jr. who provided constant insight and assisted me in my research endeavors.

I am thankful to Dr. Roger C. Sanwald and Dr. C. Richard Guarnieri for their guidance when I first began working with the group and to everyone at the Institute of Maintenance Science and Technology. I owe many thanks to the students and staff involved with the Arcam project. Also, this research would not be possible without the financial support of the Golden Leaf Foundation.

I would also like to express my appreciation to the Marine Corps Air Station Cherry Point, the Analytical Instrumentation Facility at North Carolina State University, and the Shared Materials Instrumentation Facility at Duke University for the use of their facilities and equipment.

Finally, I am grateful for the continuing love and support of my parents and sister. I also want to express thanks to all my family and friends for their encouragement and patience throughout everything. You all have contributed to the success of this paper more than you know.

Table of Contents

List of Tables	vi
List of Figures	vii
1 Introduction	1
1.1 Materials and Applications.....	1
1.2 Fabrication.....	1
1.3 Research Objectives.....	2
1.4 Referenced Literature.....	3
2 Structure and Properties of Titanium Alloys	4
2.1 Crystal Structure.....	4
2.2 Microstructure.....	6
2.3 Mechanical Properties.....	7
2.4 Effect of Impurities.....	10
2.5 Referenced Literature.....	12
3 Production of Titanium Alloys	13
3.1 Conventional Fabrication Methods.....	13
3.1.1 Forging.....	13
3.1.2 Casting.....	14
3.2 Solid Freeform Fabrication.....	15
3.2.1 Laser Additive Manufacturing.....	16
3.2.2 Electron Beam Melting.....	19
3.3 Post Processing.....	25
3.4 Referenced Literature.....	27

4	Experimental Methods.....	30
4.1	Methods of Analysis.....	30
4.1.1	Mechanical Testing.....	30
4.1.2	Scanning Electron Microscopy.....	33
4.1.3	X-Ray Diffractometry.....	35
4.2	Design of Experiments.....	37
4.3	Referenced Literature.....	40
5	Results and Analysis.....	41
5.1	Mechanical Properties.....	41
5.2	Fractography.....	45
5.3	Microscopy.....	53
5.4	Phase Analysis.....	61
5.5	Referenced Literature.....	69
6	Conclusions.....	70
6.1	Summary.....	70
6.2	Future Work.....	71
6.3	Referenced Literature.....	72

List of Tables

Table 3.1	Mechanical properties of electron beam melted Ti-6Al-4V for three different growth orientations.....	24
Table 4.1	Three post processing conditions applied to the EBM as-processed specimens.....	38
Table 5.1	Mechanical properties of electron beam melted Ti-6Al-4V products evaluated using 0.0564in ² cross-sectional area and compared against wrought and cast products.....	43
Table 5.2	Mechanical properties of electron beam melted Ti-6Al-4V products evaluated using 0.0539in ² cross-sectional area and compared against wrought and cast products.....	44
Table 5.3	Calculated 2θ values for possible reflections in the measured range.....	63
Table 5.4	Comparison of calculated and measured diffraction angles.....	64

List of Figures

Figure 2.1	Pseudo-binary phase diagram of Ti-6Al with varying vanadium composition.....	6
Figure 2.2	Micrographs of Ti-6Al-4V solution heat treated above the β transus at 1066°C and (a) water quenched ($\times 500$), (b) air cooled ($\times 250$), and (c) furnace cooled ($\times 250$).....	8
Figure 2.3	Micrographs of Ti-6Al-4V heat treated below the β transus at 954°C and (a) water quenched, (b) air cooled, and (c) furnace cooled ($\times 250$).....	9
Figure 3.1	Schematic representation of (a) typical SLS setup and (b) LENS process.....	17
Figure 3.2	Ti-6Al-4V micrograph showing a martensitic structure within columnar grains which are formed parallel to the build direction during the SLS process.....	18
Figure 3.3	Schematic representation of the electron beam melting machine.....	20
Figure 3.4	Ti-6Al-4V micrograph of columnar grain formed parallel to the build direction of electron beam melted component.....	21
Figure 3.5	Ti-6Al-4V micrograph of equiaxed grain on the cross-sectional growth plane of electron beam melted component.....	22
Figure 3.6	Schematics of rectangular tensile specimens built in the EBM machine for three different growth orientations: (a) face growth plane, (b) cross-sectional growth plane, and (c) edge growth plane.....	23

Figure 4.1	Engineering stress-strain curve typical of metals. The tensile, yield, and fracture strengths are indicated on the curve.....	31
Figure 4.2	Diagram displaying the major components of the scanning electron microscope.....	33
Figure 4.3	Schematic representation of the depth of focus in an SEM image.....	34
Figure 4.4	Example of x-ray diffraction pattern for sodium chloride powder.....	36
Figure 4.5	Dimensions of the final machined cylindrical tensile specimens built in the EBM machine.....	38
Figure 5.1	Schematic of the slightly tapered cylindrical tensile specimens after machining.....	42
Figure 5.2	Fractograph of Ti-6Al-4V tensile specimen produced via EBM showing apparent columnar structure.....	46
Figure 5.3	Fractograph of Ti-6Al-4V tensile specimen produced via EBM showing tear ridges (arrow) along apparent grain boundaries.....	47
Figure 5.4	Fractograph of Ti-6Al-4V tensile specimen produced via EBM showing mostly small equiaxed dimples and several large dimples.....	48
Figure 5.5	Fractograph of Ti-6Al-4V tensile specimen produced via EBM and β heat treated displaying a mixed mode of cleavage and dimple rupture. A cleavage fracture facet (arrow) is noted.....	49
Figure 5.6	Fractograph of Ti-6Al-4V tensile specimen produced via EBM and β heat treated displaying a mixed mode of cleavage and dimple rupture. Intergranular fracture (arrow) is observed.....	50

Figure 5.7	Fractograph of Ti-6Al-4V tensile specimen produced via EBM and β heat treated. Equiaxed and elongated dimples are indicated in regions A and B, respectively.....	51
Figure 5.8	Fractograph of Ti-6Al-4V tensile specimen produced via EBM and β heat treated. Serpentine glide ridges are shown in region A, and small equiaxed dimples occur at the lath boundary in region B.....	52
Figure 5.9	Optical micrograph of Ti-6Al-4V produced via EBM showing the columnar structure parallel to the build direction.....	55
Figure 5.10	Optical micrograph of Ti-6Al-4V produced via EBM showing the equiaxed structure at the cross-sectional ends of the columnar structure.....	56
Figure 5.11	Optical micrograph of Ti-6Al-4V produced via EBM which has been β treated showing an equiaxed grain along the growth direction.....	57
Figure 5.12	Optical micrograph of Ti-6Al-4V produced via EBM and β treated for one hour and argon gas quenched.....	58
Figure 5.13	Optical micrograph of Ti-6Al-4V produced via EBM and β treated for one hour and furnace cooled.....	59
Figure 5.14	Optical micrograph of Ti-6Al-4V produced via EBM and β treated for two hours and furnace cooled.....	60
Figure 5.15	X-ray diffraction pattern of Ti-6Al-4V produced via electron beam melting process.....	65

Figure 5.16 X-ray diffraction pattern of Ti-6Al-4V produced via EBM and β treated for one hour and argon gas quenched.....	66
Figure 5.17 X-ray diffraction pattern of Ti-6Al-4V produced via EBM and β treated for one hour and furnace cooled.....	67
Figure 5.18 X-ray diffraction pattern of Ti-6Al-4V produced via EBM and β treated for two hours and furnace cooled.....	68

Chapter 1

Introduction

1.1 Material and Applications

Titanium is a nonferrous and lightweight metal which is abundant in nature, being the ninth most plentiful element. Titanium was discovered in 1791 by the British mineralogist and chemist William Gregor. In 1910, Matthew Albert Hunter from Rensselaer Polytechnic Institute was able to separate the metal by reacting titanium tetrachloride with sodium in a steel bomb. In 1932, Wilhelm Justin Kroll of Luxembourg was able to provide a means of producing large quantities of titanium. Shortly thereafter, titanium based alloys were explored for aerospace applications, specifically aircraft engines. Today, titanium alloys are used in a variety of areas including aerospace, automotive, biomedical, chemical and nuclear engineering due to their high strength and superior corrosion resistance [1].

1.2 Fabrication

Traditionally, titanium based alloy parts are fabricated by forging or casting. However, these methods of production require expensive dies or molds. The cost per part is very high for those components produced in low quantities. New technology, known as solid freeform fabrication, aims to produce high dimensional tolerance parts with similar mechanical properties at a lower cost by melting metal powder layer by layer via an energy source. Two

competing solid freeform processes are the laser additive and electron beam melting methods. Laser additive manufacturing utilizes a laser as its energy source whereas electron beam melting uses high energy electrons. One of the main advantages of electron beam melting compared to laser sintering is its high energy conversion efficiency. Much of the input power is lost during laser enhanced processes, whereas the electron beam melting system uses nearly all of its energy input [2,3]. This new technology has high hopes from the aerospace, automobile, and biomedical industries in which many near net shape parts are needed.

1.3 Research Objectives

Most solid freeform fabrication research has focused on the titanium alloy consisting of six percent aluminum and four percent vanadium, denoted as Ti-6Al-4V. The aim of this study is to determine if the electron beam melting process with the help of post processing is a viable alternative for the production of Ti-6Al-4V by using analytical techniques to characterize the structure and properties. Post processing of Ti-6Al-4V is an important step in order to improve the mechanical properties for any production route. The effectiveness of post heat treatment on the electron beam melted components is evaluated in the present study.

1.4 Referenced Literature

- [1] C. Leyens, M. Peters (Eds.), Titanium and Titanium Alloys: Fundamentals and Applications, Wiley, Weinheim, 2003, p. 532.
- [2] J. Hiemenz, EBM Offers a New Alternative for Producing Titanium Parts and Prototypes, in: Time-Compression Technologies, vol 14, Rapid News Publications, UK, 2006.
- [3] U. Lindhe, O. Harrysson, Rapid Manufacturing with Electron Beam Melting (EBM) – A manufacturing revolution, in: SME Direct Metal Fabrication Forum, Dearborn, Michigan, USA, 2003, p. 6.

Chapter 2

Structure and Properties of Titanium

Alloys

Titanium alloys are classified into three sectors according to the phases present: α , $\alpha+\beta$, and β alloys. The $\alpha+\beta$ alloys are the most commonly used due to a wide range of excellent material properties. The $\alpha+\beta$ alloys consist of an α and at least one β stabilizing element. The most common α stabilizing elements include aluminum, oxygen, nitrogen, and carbon, and the most common β stabilizers are molybdenum, vanadium, chromium, niobium, copper, and iron. The "workhorse" of the titanium alloys is the $\alpha+\beta$ titanium alloy consisting of six percent of the α stabilizer aluminum and four percent of the β stabilizer vanadium and is denoted as Ti-6Al-4V [1-5].

2.1 Crystal Structure

The α phase has a hexagonal close packed (hcp) crystal structure, and the β phase is a body centered cubic (bcc) structure. The hcp crystal structure is anisotropic, meaning the physical properties depend on the direction in which they are measured. Therefore, the material properties will greatly depend on the preferred orientation, or crystallographic texture, of the α grains, which is determined by the processing history [1-5].

In the $\alpha+\beta$ alloy Ti-6Al-4V, the addition of aluminum provides additional strength of the α phase. Vanadium is added to stabilize the β phase which improves the ability for the material to plastically deform. Slip deformation is more energetically favorable in bcc crystals than hcp because it has a shorter path length. According to Von Mises criterion, a minimum of five independent slip systems is needed in order to have homogeneous plastic deformation. In the case of hexagonal close packed structure, there are a total of four independent slip systems which makes the α (hcp) titanium difficult to plastically deform. The introduction of the β (bcc) phase in Ti-6Al-4V gives rise to additional independent slip systems which improves the ductility [1-5].

The transformation from the β phase to the α phase upon cooling occurs as the close packed slip planes of the β (bcc) titanium transform to the basal planes of the α (hcp) titanium. The final transformation from the α to β phase is slightly distorted due to the differences in atomic distances between the $\{0001\}$ basal plane of the α (hcp) and the $\{110\}$ diagonal close packed plane of the β (bcc). The \mathbf{a} axis of the hcp is expanded, and the \mathbf{c} axis is contracted thereby reducing the \mathbf{c}/\mathbf{a} ratio of the α titanium below the value for an ideally close packed hexagonal lattice. The burgers relationship between the slip planes and slip directions for the phase transformation is given below:

$$\begin{aligned} \{0001\}_{\alpha} // \{110\}_{\beta} \\ \langle 1120 \rangle_{\alpha} // \langle 111 \rangle_{\beta} \end{aligned}$$

From this relationship, there are a total of 12 variants of orientation which are a result of the six close packed planes and the two slip directions of the β titanium unit cell. A "basket weave" structure is evident in the microstructure as the lamellar structure grows in the orientation of these 12 variants [1].

2.2 Microstructure

In view of the equilibrium phase diagram, the final microstructure may be predicted when considering the chemical composition, processing history, and post processing heat treatment. The diagram in Figure 2.1 is the pseudo-binary phase diagram of Ti-6Al with varying vanadium composition.

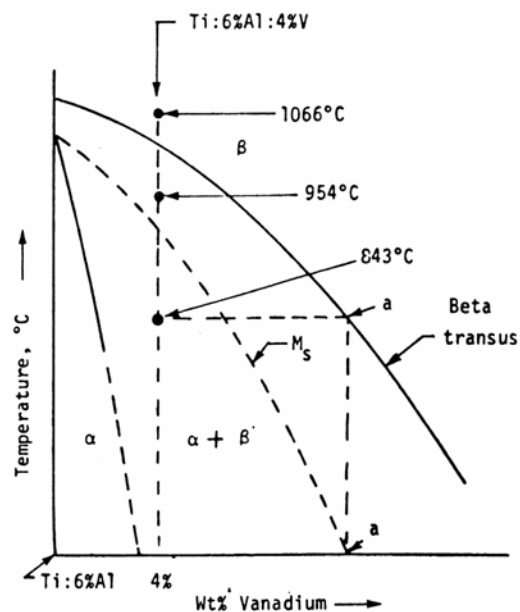


Figure 2.1: Pseudo-binary phase diagram of Ti-6Al with varying vanadium composition [4].

At four percent vanadium, water quenching from above the β transus temperature produces hcp titanium martensite (α') by a diffusionless phase transformation process. The microstructure of α' martensite consists of needle-like platelets which are heavily twinned. The titanium martensite increases the strength by grain refinement and by increased

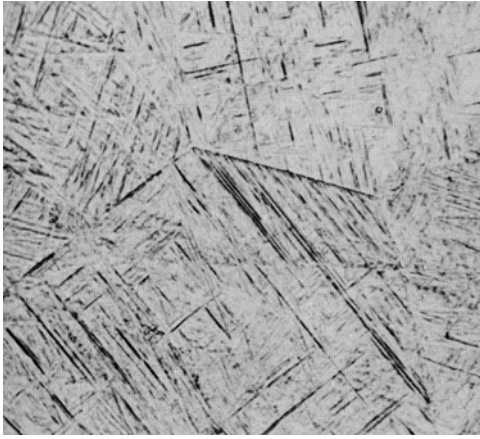
dislocation density due to the rapid transformation. When air cooled from above the β transus temperature, acicular α is formed from the β phase by nucleation and growth. Slow furnace cooling from above the β transus temperature will produce coarse plate-like α structure with some intergranular β due to the slow cooling rate [1-5]. Figure 2.2 shows examples of microstructures cooled from the β region at different rates.

Cooling from the $\alpha+\beta$ region yields slightly different microstructures and mechanical properties. When Ti-6Al-4V is quenched just below the β transus, the β phase is transformed to α' and the primary α remains. Air cooling in the same region produces primary α in a transformed β matrix which is acicular. An equiaxed α structure containing intergranular β is formed by furnace cooling from the $\alpha+\beta$ region [1-5]. Figure 2.3 shows examples of microstructures cooled from the $\alpha+\beta$ region at different rates.

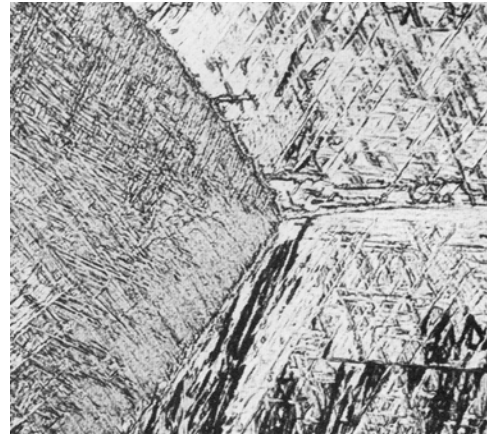
2.3 Mechanical Properties

The mechanical properties of titanium alloys are highly dependent on the phase composition and microstructure. Near α titanium alloys exhibit increased strength and high creep resistance due to the limited volume diffusion in the hcp crystal structure. On the other hand, the β titanium alloys provide excellent toughness and fatigue properties due to ease of plastic deformation. The presence of both the α and β phases in Ti-6Al-4V enhances the range of good mechanical properties which is why this alloy makes up more than 50% of all performance alloys [1-3].

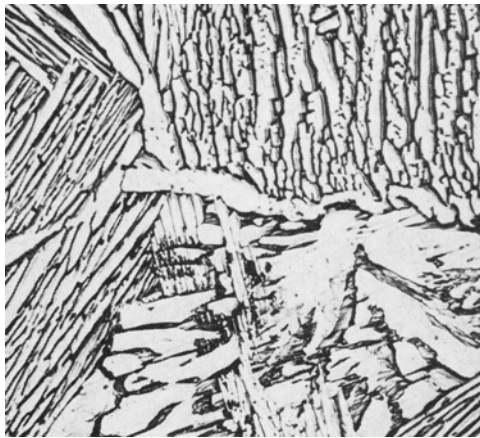
Titanium alloys may be tailored to the desired mechanical properties by altering the microstructure by means of thermal processing and/or deformation. The grain size, grain shape, and their arrangements define the resulting mechanical behavior. The macrostructure



(a)



(b)

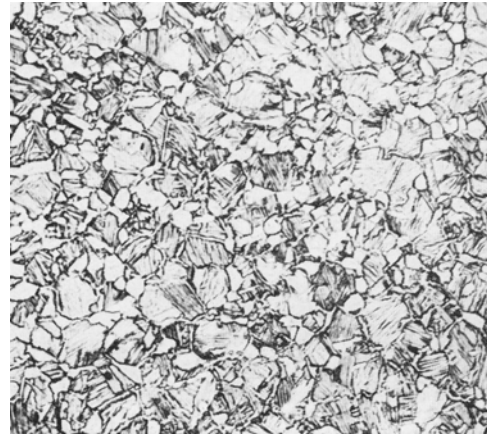


(c)

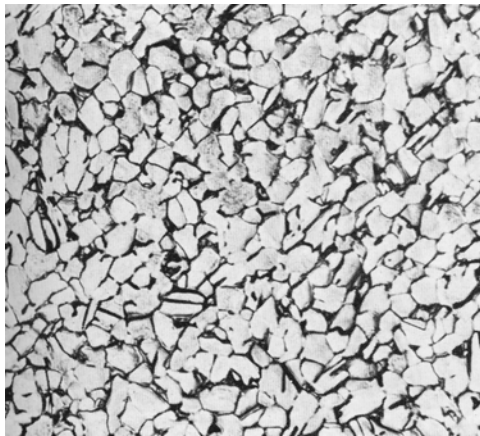
Figure 2.2: Micrographs of Ti-6Al-4V solution heat treated above the β transus at 1066°C and (a) water quenched ($\times 500$) [4], (b) air cooled ($\times 250$), and (c) furnace cooled ($\times 250$) [5].



(a)



(b)



(c)

Figure 2.3: Micrographs of Ti-6Al-4V heat treated below the β transus at 954°C and (a) water quenched, (b) air cooled, and (c) furnace cooled. ($\times 250$) [5].

grain size influences the strength of the material. Separate studies by Hall and Petch showed that smaller grain sizes provide higher yield strength by inhibiting dislocation motion. The yield stress increases because there are more boundaries to block the movement of dislocations during deformation. The Hall-Petch relationship is given by Equation 2.1, where σ_y represents the yield strength, d is the grain diameter, and σ_0 and K are constants.

$$\sigma_y = \sigma_0 + \frac{K}{\sqrt{d}} \quad (2.1)$$

The yield strength (σ_y) is inversely related to the grain diameter (d) [6,7]. Also, small grain size in the Ti-6Al-4V alloy improves the fracture toughness since large grains provide long intergranular fracture paths at the grain boundary [3].

The microstructure of the α phase affects the mechanical behavior as well. Several α morphologies may emerge depending on the processing history. A fine equiaxed microstructure provides excellent strength, and large equiaxed α grains offer the greatest ductility. Although not as great as the equiaxed structure, good strength may be obtained from a fine acicular α structure, and soft, ductile properties are seen in coarse lamellar structures. A bimodal distribution of equiaxed and lamellar structures offers the best combination of tensile properties [1,3,8].

2.4 Effect of Impurities

Interstitial impurities in titanium alloys include carbon, oxygen, nitrogen, and hydrogen. Carbon, oxygen, and nitrogen are α stabilizers, and hydrogen stabilizes the β phase. The mechanical properties of titanium alloys are especially sensitive to hydrogen uptake at elevated temperatures. Hydrogen is a well known deterrent for alloy ductility. Hydrogen

causes embrittlement of titanium alloys by precipitating titanium hydrides when the hydrogen content increases above a critical value. In $\alpha+\beta$ titanium alloys, these hydrides precipitate more easily due to the lower hydrogen solubility in the α phase. By using an alloy grade of low hydrogen content and by processing in vacuum or an inert atmosphere, hydrogen embrittlement may be prevented [3,8].

2.5 Referenced Literature

- [1] C. Leyens, M. Peters (Eds.), Titanium and Titanium Alloys: Fundamentals and Applications, Wiley, Weinheim, 2003, p. 532.
- [2] J. C. Williams, Titanium alloys: production, behavior and application, in: H. M. Flower (Ed.) High Performance Materials in Aerospace, Chapman & Hall, Cambridge, 1995, pp. 85-134.
- [3] J. Matthew J. Donachie (Ed.) Titanium: A Technical Guide, ASM, Metals Park, 2000, p. 381.
- [4] W. F. Smith, Titanium and Its Alloys, in: Structure and Properties of Engineering Alloys, McGraw-Hill, New York, 1993, p. 630.
- [5] Titanium and Titanium Alloys, in: Metals Handbook, vol 9, ASM, Metals Park, 1985, pp. 458-475.
- [6] E. O. Hall, Proceedings of the Physical Society of London Section B 64 (1951) 747-753.
- [7] N. J. Petch, Journal of the Iron and Steel Institute 174 (1953) 25-28.
- [8] R. J. McClintick, W. C. Bauer, L. S. Busch, Physical Metallurgy and Heat Treatment of Titanium Alloys, Mallory-Sharon, Niles, OH, 1955, p. 60.

Chapter 3

Production of Titanium Alloys

Titanium components are most commonly produced by forging because the microstructure may be easily controlled by deformation and heat treatment. Investment casting is implemented for manufacturing complex shapes and/or expensive parts [1]. The latest technology for creating near net shape components involves melting metal powder using a laser or electron source.

3.1 Conventional Fabrication Methods

3.1.1 Forging

Forging is used for the fabrication of titanium alloy components because large cross sections and near net shape parts may be created while controlling the microstructure by thermomechanical processing. The resulting microstructure of forged products depends primarily on the forging temperature, rate of deformation, and cooling rate. The final microstructure also depends on the microstructure of the starting material. The process of producing forging stock begins with cylindrical ingot casts which have been vacuum arc remelted and then hand forged to the desired billet shape. Forging above or below the β transus breaks up the large grain as-cast microstructure and helps to obtain a more desirable equiaxed structure. Additional forging in the $\alpha+\beta$ region is needed to achieve the final microstructure and dimensions for the die forging process [1-3].

The selected secondary die forging process depends on the preferred microstructure. Forging at temperatures above the β transus produces a colony microstructure which is characterized by clusters of α plates growing in the same direction. These α plates are known to improve the fracture toughness greatly but reduce the fatigue properties. The microstructure may also consist of a continuous α phase at prior β grain boundaries which gives unfavorable mechanical properties. Another major concern associated with β processing is hydrogen pick up which occurs at high temperatures and leads to hydrogen embrittlement. Forging at temperatures in the $\alpha+\beta$ region results in a fine equiaxed primary α structure which provides excellent strength and ductility [1-3]. However, several types of fracture defects may develop from working in the $\alpha+\beta$ region. Such defects include strain-induced porosity, wedge cracking at the triple points of β grain boundaries, and the formation of microvoids as a result of high strain rates. In order to avoid cracking, forging in the $\alpha+\beta$ region is done at 30°C to 100°C below the β transus [3].

One of the major issues with forging titanium is non-uniform heating due to its low conductivity. Shear cracking is a concern for $\alpha+\beta$ titanium alloys when working in either the β or $\alpha+\beta$ region. This type of defect is caused by non-uniform deformation of the workpiece as a result of the non-uniform heating. Shear bands or shear cracks occur between regions of low and high deformation [3].

3.1.2 Casting

Near net shape parts which are too expensive or complex for forging are produced by casting, although the strength and ductility are sacrificed. Studies of investment casting have shown to give the best possible mechanical properties of cast titanium alloys [1,4].

Titanium cast products are formed by melting the alloy in a vacuum furnace or in an inert atmosphere since titanium is highly reactive at high temperatures. The molten metal is poured into a mold of the desired shape. The resultant macrostructure consists of columnar grains solidified from the mold walls and equiaxed grains toward the center [1,4].

Casting of titanium can be difficult since it offers low fluidity and high reactivity thereby leading to casting defects like porosity, shrinkage cavities, and surface defects. Careful selection of the molding materials is required so that the reaction between the molding materials and the molten titanium is limited. Oxide molds such as Al_2O_3 and ZrO_2 are common investment casting materials for Ti-6Al-4V [4]. However, it is impossible to completely eliminate reactions at the metal-mold interface, and the as-cast material will comprise of an outer layer of unfavorable constituents known as α case. This brittle layer is detrimental to the mechanical properties and must be removed by pickling or machining [1,4]. Ways in which the α case layer thickness may be decreased include increasing the cooling rate, decreasing the temperature of the molten metal, and not preheating the mold [4].

3.2 Solid Freeform Fabrication

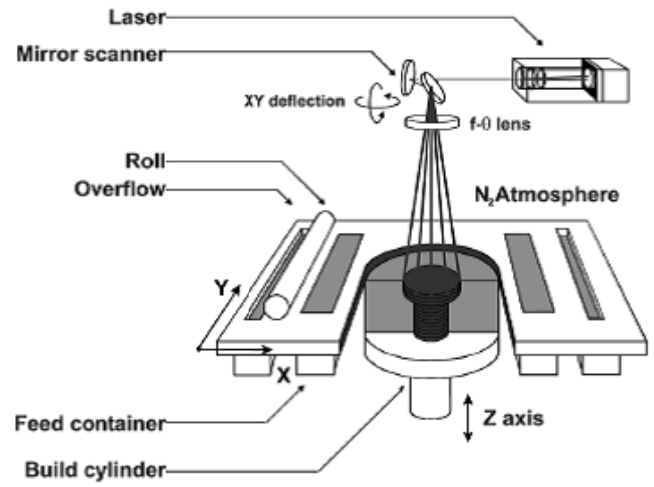
Solid freeform fabrication is a new method of producing titanium alloys. High dimensional tolerance parts may be produced because the components are built in a layer by layer fashion with alloy powder. Laser additive and electron beam melting methods have been the recent focus for the fabrication of Ti-6Al-4V near net shape parts. These processes are similar in that both use a focused energy source to melt the alloy powder. One of the main advantages of electron beam melting compared to laser sintering is its high energy conversion efficiency. Laser sintering converts only a small amount of input power to useable work, whereas the electron beam melting system uses nearly all of its energy input [5,6].

3.2.1 Laser Additive Manufacturing

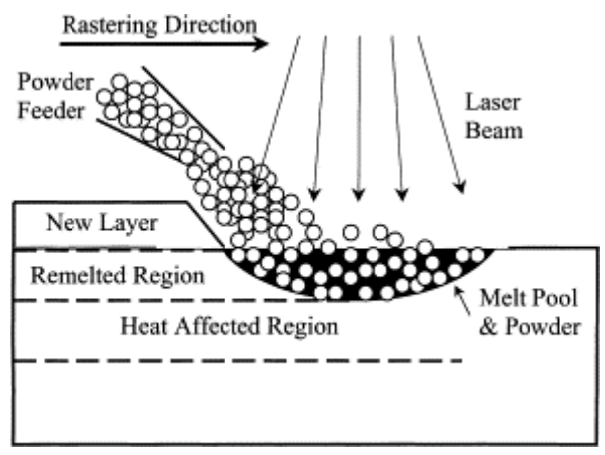
Laser additive manufacturing utilizes a high power laser (CO₂ or Nd-YAG) as a heat source in addition to a computer aided design model for building near net shape components from powdered material in a layer by layer fashion. Typically, this process is performed in an inert atmosphere, such as argon, to reduce oxidation effects. Selective Laser Sintering (SLS) and Laser Engineered Net Shaping (LENS) are the two foremost laser based fabrication technologies. These processes are similar in that they both raster the desired areas of the powder bed one layer at a time. The layer thickness usually ranges between 50 and 200 microns, depending on the powder size and material. After rastering of one layer is complete, a new layer of powder is spread across the previous layer, and the process is repeated until completion of the final shape [7-9]. Figure 3.1 illustrates how the SLS and LENS systems operate.

The LENS process differs from SLS because it has the ability to feed powder into the melt pool produced by the laser, therefore alloy composition may be adjusted where needed. Originally, high dimensional tolerance parts using SLS were built for manufacturing polymeric materials, but the process since has broadened its use for producing steels, nickel-based alloys, and α/β titanium alloys [8,9].

The final product contains a rough surface due to the part being in contact with the loose powder. This is easily resolved by machining the surface of the part, which must be built with slightly larger dimensions in order to compensate for material loss during machining. As seen in Figure 3.2, the resultant microstructure of materials fabricated by laser additive manufacturing consists of a columnar structure or a mixed columnar and equiaxed structure. The columnar grains form parallel to the build direction due to the directional solidification effect [7,8,12-14].



(a)



(b)

Figure 3.1: Schematic representation of (a) typical SLS setup [10] and (b) LENS process [11].

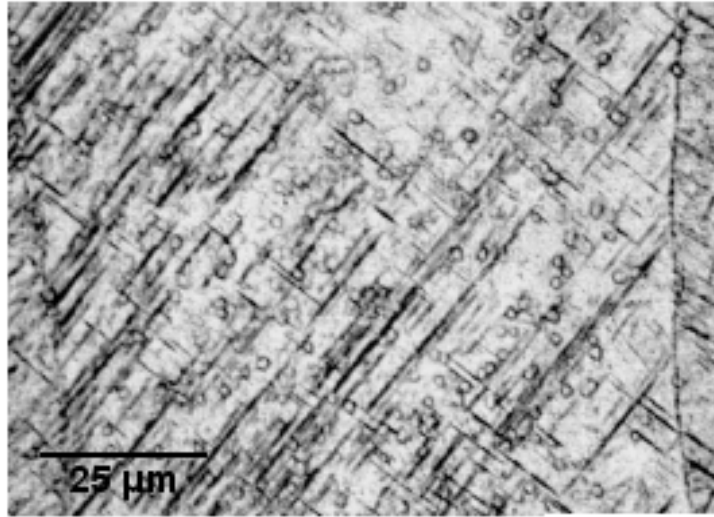


Figure 3.2: Ti-6Al-4V micrograph showing a martensitic structure within columnar grains which are formed parallel to the build direction during the SLS process [14].

The microstructure changes when the processing parameters such as laser power and traverse speed are varied. An increase in the traverse speed results in faster cooling thereby reducing the grain width and refining the microstructure. An increase in the incident energy (laser power divided by traverse speed) results in larger grain size and coarse microstructure. Therefore, a high power and low traverse speed will result in large grains, and a low power and high traverse speed will result in smaller grain size [12-15].

Two types of porosity may occur in these processes: lack of fusion and gas porosity. The porosity caused by lack of fusion increases when the laser power decreases or the traverse speed increases. Conversely, gas porosity increases when the laser power increases or the traverse speed decreases. It is possible that gas porosity is created by trapped gas from the shielding gas or from the evaporation of alloying elements [8,13], and some even suggest that

it may be associated with the type of CO₂ laser used [15]. Processing parameters must be aptly adjusted in order to obtain adequate densification of the component. For Ti-6Al-4V alloys, there is a small processing window for optimizing these parameters, and careful consideration is required to ensure that the laser power and traverse speed yield a suitable incident energy for the best densification [13,15].

3.2.2 Electron Beam Melting

Electron Beam Melting (EBM) is similar to laser additive manufacturing in that near net shape components are built in a layer by layer fashion. The difference is that an electron beam is used as an energy source rather than a laser. Electron beam melted parts are produced in vacuum at around 10^{-3} Torr, which makes it ideal for highly reactive metals like titanium. The electron beam melting process begins with a 100 micron thick layer of powder spread across a steel start plate. Electrons are produced by thermionic emission of a tungsten filament and are accelerated through the gun. An electromagnetic lens focuses the electrons to a specified diameter while another deflects the focused beam to the target point on the powder bed [5,6]. Figure 3.3 shows a schematic representation of the EBM machine.

Initially, the powder is lightly sintered by scanning the pattern at a relatively low beam current and high beam velocity. The next step is to melt the powder by increasing the beam current while decreasing the beam velocity. As the fast-moving electrons strike the metal powder, the kinetic energy is converted into thermal energy. The high beam current and low beam velocity allows more heat per area per time [16]. When the temperature reaches the melting point, the electron beam rapidly liquefies the powder layer. Subsequent layers are built on the former, and the electron beam continues to raster the desired areas until the near net shape component is complete [5,6].

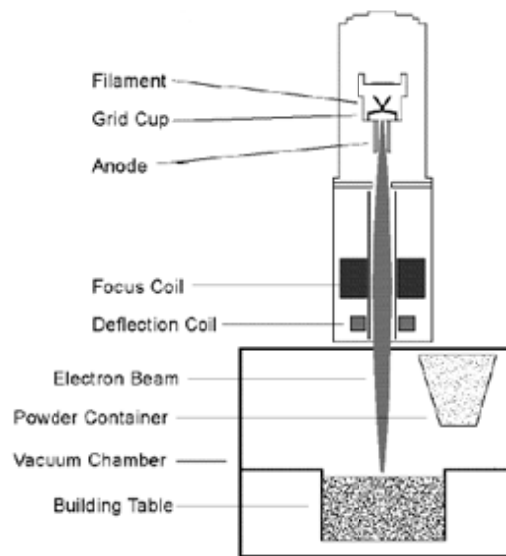


Figure 3.3: Schematic representation of the electron beam melting machine [5].

Studies conducted prior to the current investigation revealed the same columnar macrostructure observed in the laser assisted solid freeform fabrication system. The columnar structure was parallel to the growth direction, and an equiaxed structure was seen on the cross-sectional growth plane. This is illustrated in Figures 3.4 and 3.5. Tensile tests were performed, as well, on rectangular tensile specimens with a two-inch gage length, built according to ASTM E8. The specimens were built for three different growth orientations which are illustrated in Figure 3.6.

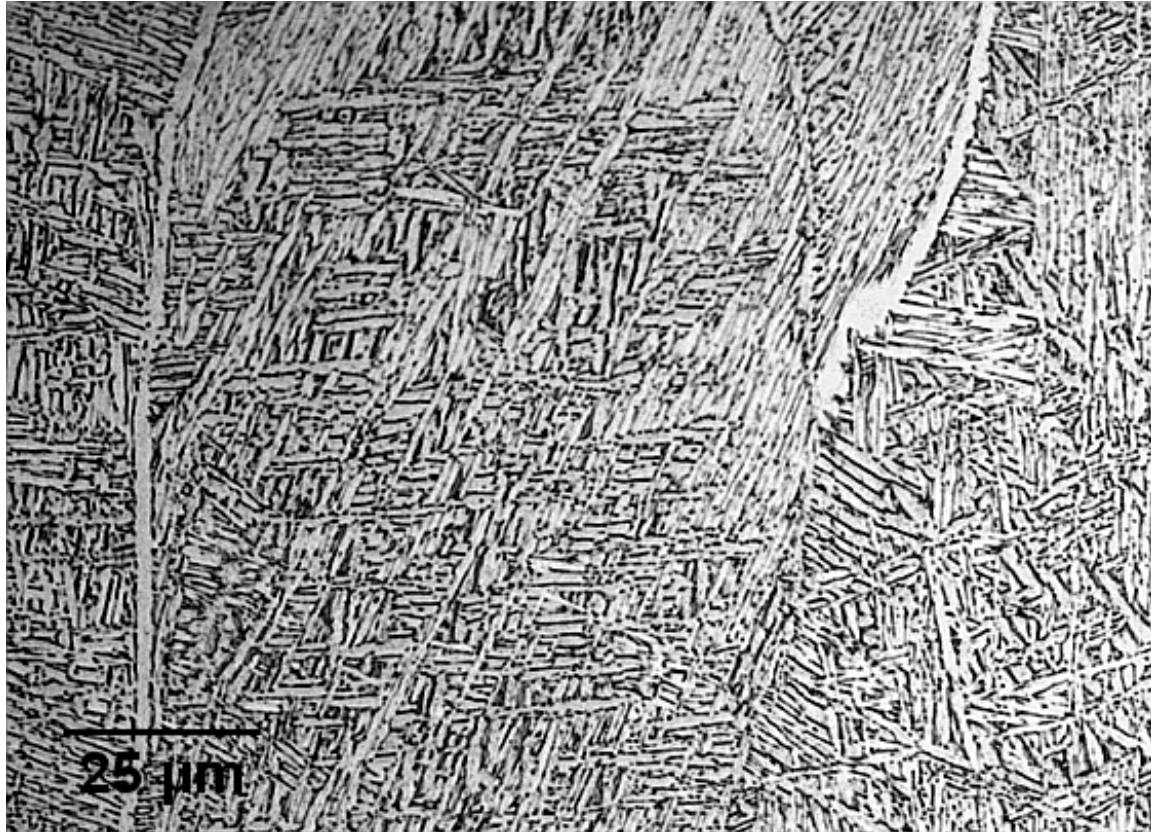


Figure 3.4: Ti-6Al-4V micrograph of columnar grain formed parallel to the build direction of electron beam melted component.

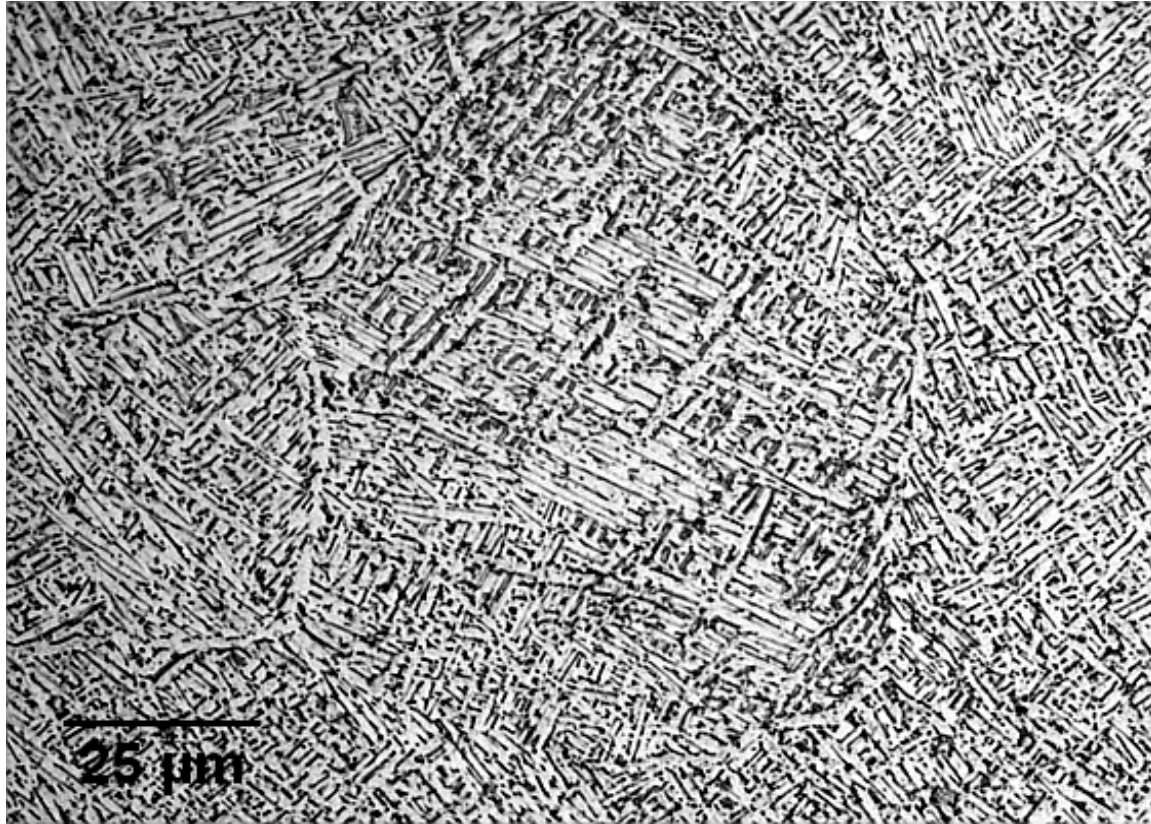


Figure 3.5: Ti-6Al-4V micrograph of equiaxed grain on the cross-sectional growth plane of electron beam melted component.

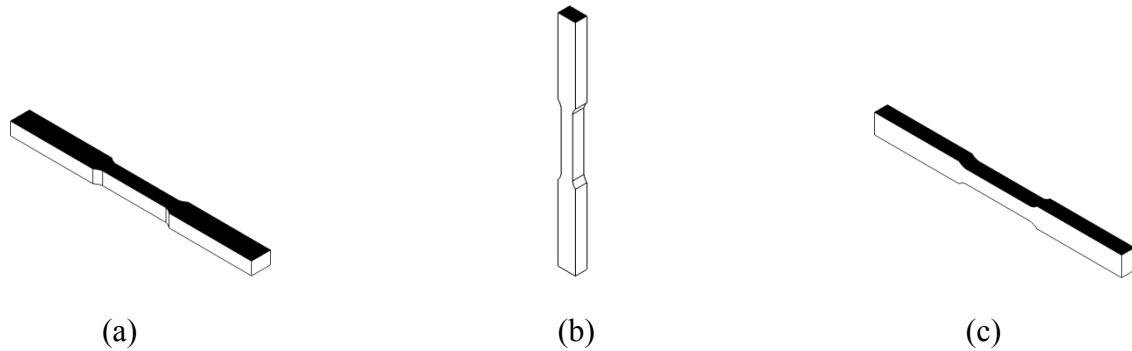


Figure 3.6: Schematics of rectangular tensile specimens built in the EBM machine for three different growth orientations: (a) face growth plane, (b) cross-sectional growth plane, and (c) edge growth plane.

The average values for the ultimate tensile strength, yield strength, and percent elongation for the three different growth planes are presented in Table 3.1. A significant difference in tensile properties is found in the edge growth plane specimens, particularly the percent of elongation which is increased by a sizable margin. It is possible that the differences in macrostructure due to the directional solidification effect contributes to the anisotropy of tensile properties, or preferred orientation of the α laths may play a role as well.

As with laser aided manufacturing, the final electron beam melted part has a rough surface, which must be removed by machining. Cormier et al suggested a post-processing step for improving the surface quality which involves removing the loose powder and "glazing" the surface with the electron beam. It was demonstrated that scanning the beam perpendicular to the direction of the build layers reduces the surface roughness by 96.7% when compared to the original surface [16].

Table 3.1: Mechanical properties of electron beam melted Ti-6Al-4V for three different growth orientations.

		UTS (MPa)	YS (MPa)	%EL
Growth Plane				
1	Face (Growth Plane Normal to Tensile Axis)	1052	973	8
2	Cross-section (Growth Plane Parallel to Tensile Axis)	1082	1028	8
3	Edge (Growth Plane Normal to Tensile Axis)	1082	959	15

Like the laser additive manufacturing methods, porosity exists which may be attributed to lack of fusion and entrapped gas. Build speed plays an important role in the densification of EBM parts. For metals, fabrication is accomplished at beam velocities of approximately 500 mm/sec. At faster beam velocities, the melted powder does not have time to flow and completely sinter thus creating pores within the material [16]. Entrapped gas produced by the volatilization of alloying elements is more concerning for the EBM system since fabrication takes place under high vacuum. Evaporation of elements is a common problem in other processes involving a thin melt pool and high vacuum (i.e., thin film technology, vacuum metallurgy, etc.). Evaporation of alloying elements not only leads to gas porosity but also presents challenges for controlling the chemical composition. In Ti-6Al-4V, the depletion of aluminum is most concerning because of its high vapor pressure [17]. As with laser assisted

freeform fabrication, the processing parameters must be optimized in order to achieve adequate densification.

3.3 Post Processing

Post processing methods are necessary for the optimization of alloy properties. For example, hot isostatic pressing (HIP) is used to improve the strength by eliminating voids which arise from residual shrinkage during solidification. For Ti-6Al-4V components, a standard HIP process occurs around 900°C with an applied pressure of 100 MPa. Hot isostatic pressing allows the material to undergo slight creep deformation in order to relieve cavity stresses but does not change the overall part geometry [1]. This post processing technique is commonly performed after casting, and more recently has been included in the solid freeform fabrication process regime [18].

In order to tailor the microstructure for specific mechanical requirements, various heat treatments are carried out. Time and temperature of the thermal treatment and the cooling rate are the critical factors affecting the final microstructure. In two phase $\alpha+\beta$ alloys, high strengths and adequate ductility are obtained by heat treating high in the $\alpha+\beta$ field to produce a bimodal microstructure of large equiaxed α grains in an acicular transformed β matrix [1,2,19,20]. A soft, ductile microstructure also is produced after slowly cooling from the β region, although the ductility is not as great as $\alpha+\beta$ heat treatments [21]. Processing above the β transus typically is done for improving the fracture toughness by creating colonies of α lamellae, which slow the propagation of cracks. As the crack growth front crosses from one colony to another colony of a different orientation, the crack growth changes direction by secondary crack formation or crack branching which requires more

energy thereby delaying crack propagation. The fracture toughness is increased with more colonies of α lamellae [1,2,20,22]. A disadvantage of heat treating above the β transus is the loss of ductility caused by coarsening of the continuous α grain boundary which promotes crack nucleation and fracture as a result of localized strain along the α boundary [1,2,19,20].

The current research aims to improve the tensile properties, specifically ductility, of the EBM as-processed components by post heat treatment. Although some loss of ductility is seen in β heat treatments, the current study anticipates improved ductility of the EBM components after processing in this region for two reasons:

1. Because preferential growth of α laths occurs due to directional solidification effects, an increase in ductility is expected after β heat treating to remove any preferred orientation by reformation of α grains.
2. An improvement in the tensile properties is possible if, upon cooling from the β region, new grain boundaries form to disunite the columnar macrostructure.

3.4 Referenced Literature

- [1] C. Leyens, M. Peters (Eds.), Titanium and Titanium Alloys: Fundamentals and Applications, Wiley, Weinheim, 2003, p. 532.
- [2] J. C. Williams, Titanium alloys: production, behavior and application, in: H. M. Flower (Ed.) High Performance Materials in Aerospace, Chapman & Hall, Cambridge, 1995, pp. 85-134.
- [3] S. L. Semiatin, V. Seetharaman, I. Weiss, Journal of the Minerals Metals & Materials Society 49 (1997) 33-39.
- [4] L. Nastac, M. N. Gungor, I. Ucok, K. L. Klug, W. T. Tack, International Journal of Cast Metals Research 19 (2006) 73-93.
- [5] J. Hiemenz, EBM Offers a New Alternative for Producing Titanium Parts and Prototypes, in: Time-Compression Technologies, vol 14, Rapid News Publications, UK, 2006.
- [6] U. Lindhe, O. Harrysson, Rapid Manufacturing with Electron Beam Melting (EBM) – A manufacturing revolution, in: SME Direct Metal Fabrication Forum, Dearborn, Michigan, USA, 2003, p. 6.
- [7] A. Simchi, F. Petzoldt, H. Pohl, International Journal of Powder Metallurgy 37 (2001) 49-61.
- [8] G. K. Lewis, E. Schlienger, Materials & Design 21 (2000) 417-423.
- [9] P. L. Blackwell, A. Wisbey, Journal of Materials Processing Technology 170 (2005) 268-276.

- [10] J. P. Kruth, P. Mercelis, J. Van Vaerenbergh, L. Froyen, M. Rombouts, *Rapid Prototyping Journal* 11 (2005) 26-36.
- [11] M. Grujicic, G. Cao, R. S. Figliola, *Applied Surface Science* 183 (2001) 43-57.
- [12] J. Mazumder, A. Schifferer, J. Choi, *Materials Research Innovations* 3 (1999) 118-131.
- [13] P. A. Kobryn, E. H. Moore, S. L. Semiatin, *Scripta Materialia* 43 (2000) 299-305.
- [14] P. A. Kobryn, S. L. Semiatin, *Journal of the Minerals Metals & Materials Society* 53 (2001) 40-42.
- [15] X. Wu, J. Mei, *Journal of Materials Processing Technology* 135 (2003) 266-270.
- [16] D. Cormier, Optimization of the electron beam melting process, in: *IIE Annual Conference and Expo*, Houston, Texas, USA, 2004.
- [17] S. Watakabe, K. Suzuki, K. Nishikawa, *ISIJ International* 32 (1992) 625-629.
- [18] S. Das, M. Wohler, J. J. Beaman, D. L. Bourell, *Materials & Design* 20 (1999) 115-121.
- [19] W. F. Smith, *Titanium and Its Alloys*, in: *Structure and Properties of Engineering Alloys*, McGraw-Hill, New York, 1993, p. 630.
- [20] J. Matthew J. Donachie (Ed.) *Titanium: A Technical Guide*, ASM, Metals Park, 2000, p. 381.
- [21] R. J. McClintick, W. C. Bauer, L. S. Busch, *Physical Metallurgy and Heat Treatment of Titanium Alloys*, Mallory-Sharon, Niles, OH, 1955, p. 60.

- [22] R. Filip, K. Kubiak, W. Ziaja, J. Sieniawski, *Journal of Materials Processing Technology* 133 (2003) 84-89.

Chapter 4

Experimental Methods

Ti-6Al-4V samples were produced by the solid freeform electron beam melting technique. The microstructure of the as-processed samples was altered through post heat treating in order to improve upon the mechanical properties, specifically the ductility. Several analytical techniques were used to compare the as-processed samples to those which were heat treated. The following sections explain the methods used for analysis and the overall design of experiments.

4.1 Methods of Analysis

4.1.1 Mechanical Testing

Tension tests are used in the evaluation of mechanical alloys for determining the strength and ductility. A standard tensile specimen is mounted in a testing apparatus which applies a uniaxial tensile load. An extensometer, which is equivalent or smaller than the specimen gage length, is attached to the specimen in order to measure the elongation during testing. The specimen is elongated at a constant rate until fracture occurs. The tensile test measures the load (force) against the elongation (displacement) and then converted to an engineering stress-strain curve, as seen in Figure 4.1, for determining valuable mechanical properties [1].

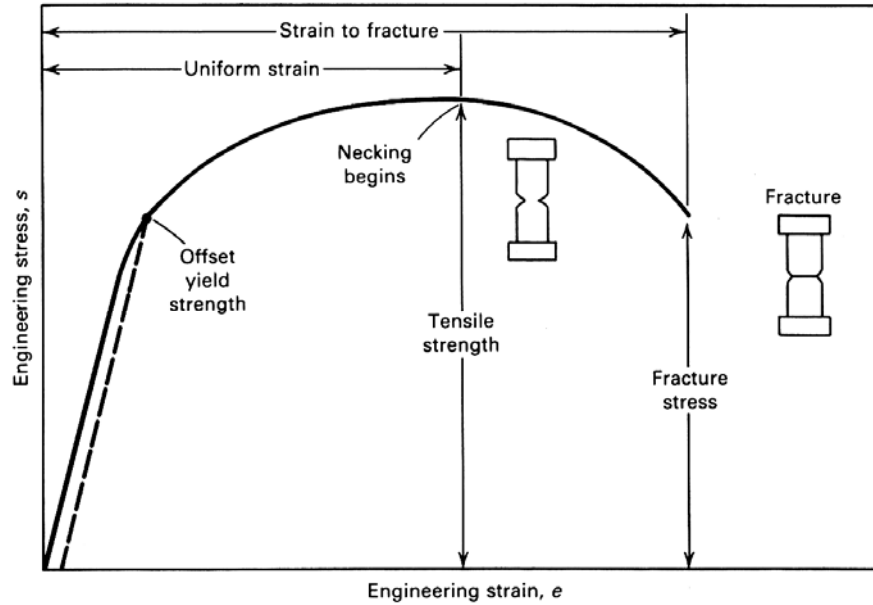


Figure 4.1: Engineering stress-strain curve typical of metals. The tensile, yield, and fracture strengths are indicated on the curve [1].

The force is converted to engineering stress by the following relationship in which F is the applied load and A_0 is the original cross-sectional area of the specimen.

$$\sigma = \frac{F}{A_0} \quad (4.1)$$

Engineering strain is known by the following equation, where Δl is the elongation and l_0 is the initial gage length [1].

$$\varepsilon = \frac{\Delta l}{l_0} \quad (4.2)$$

The mechanical strength values specified for engineering design purposes include tensile and yield strength. The tensile strength is the maximum stress that a material can withstand while in tension, therefore it is determined by the maximum stress on the engineering stress-strain curve. The yield strength is the stress at which elastic deformation ends and plastic deformation begins. Because yielding in metals is a gradual transition, a 0.2% strain offset is used to resolve the yield strength. By the offset method, a line is drawn parallel to the elastic region of the stress-strain curve from the 0.002 strain offset, and the point at which the line intersects the stress-strain curve is defined as the yield strength (Figure 4.1) [1].

Another important mechanical property is ductility which is measured by percent elongation or area reduction. The elongation is measured using the extensometer, whereby the final displacement measurement (Δl) is divided by the extensometer gage length (l_0).

$$\%EL = \frac{\Delta l}{l_0} \times 100\% \quad (4.3)$$

The area reduction is determined by fitting the fractured tensile specimen back together and measuring the diameter from which the cross sectional area after fracture (A_f) is calculated. The change in the cross sectional area divided by the original cross sectional (A_0) area gives the reduction in area [1].

$$\%RA = \frac{A_0 - A_f}{A_0} \times 100\% \quad (4.4)$$

The mechanical properties were evaluated using an RSL tension testing machine and an Epsilon one-inch extensometer. From the data collected, the tensile and yield strengths were calculated, as well as the percent elongation and percent reduction in area.

4.1.2 Scanning Electron Microscopy

Scanning electron microscopy (SEM) is a form of microscopy by which a focused electron beam rasters the area of interest to form an image via detection of secondary and/or backscattered electrons. Images obtained in the SEM appear to be three-dimensional due to its large depth of focus. SEM imaging capabilities are dependent on the beam parameters and electron optical alignment, which are all interrelated [2]. The major components of an SEM include an electron gun and a set of electromagnetic lenses which are illustrated in Figure 4.2 below.

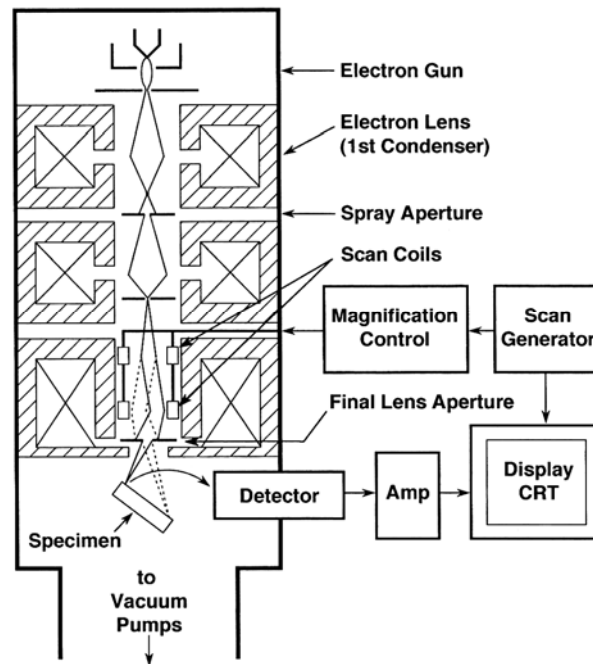


Figure 4.2: Diagram displaying the major components of the scanning electron microscope [2].

The microscope column is evacuated so that the electrons have a free path to the sample. The emitted electrons are accelerated through the electron gun and focused to the anode. The beam crossover is demagnified by a pair of condenser lenses to obtain the desired spot size. An objective aperture may be inserted for further demagnification. Below the objective aperture is the objective lens which focuses the beam onto the sample [2].

Essentially, there are three operator controls of SEM lenses: beam current (condenser lens strength), working distance, and aperture size. The beam current controls the final spot size. A strong condenser lens current reduces the spot size which is important for high resolution imaging, although the signal to noise ratio is compromised. A small working distance is also ideal for high resolutions since a smaller working distance allows for greater demagnification of spot size. Longer working distances are needed when a larger depth of focus is desired, however the image resolution diminishes. The depth of focus is improved by the smaller convergence angle achieved at longer working distances. Figure 4.3 illustrates how a smaller convergence angle allows more image features at varying heights to appear in focus [2].

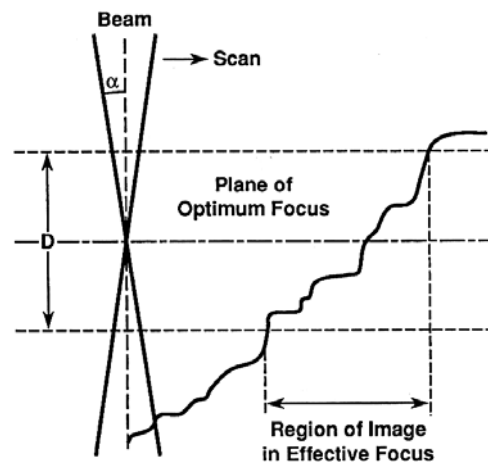


Figure 4.3: Schematic representation of the depth of focus in an SEM image [2].

The third operator control of the SEM is the aperture size. The aperture size controls the final beam current as well as the convergence angle. A smaller aperture size means a lower beam current and smaller convergence angle which lowers the signal to noise ratio but improves both the resolution and depth of focus [2].

The Hitachi S-3200N scanning electron microscope is used to obtain secondary electron images of the fractured tensile specimens. For optimal focus, fractographs are obtained using conditions for a large depth of focus (i.e., long working distance and small objective aperture).

4.1.3 X-Ray Diffractometry

X-ray diffraction is used to determine the phases present in the material and their relative amounts. Diffraction occurs in solids as waves interact with a crystalline structure and constructively interfere producing a diffracted beam. At a specified wavelength, diffraction occurs at a particular angle that depends on the interatomic spacing of the material. Bragg's law, defined below, must be satisfied in order for diffraction to occur.

$$n\lambda = 2d\sin\theta \quad (4.5)$$

In Equation 4.5, n is an integer, λ is the wavelength used, d is the interplanar spacing, and θ is the diffraction angle [3].

The intensity of the diffraction peaks are plotted against twice the diffraction angle (2θ). An example of an x-ray diffraction spectrum is seen in Figure 4.4.

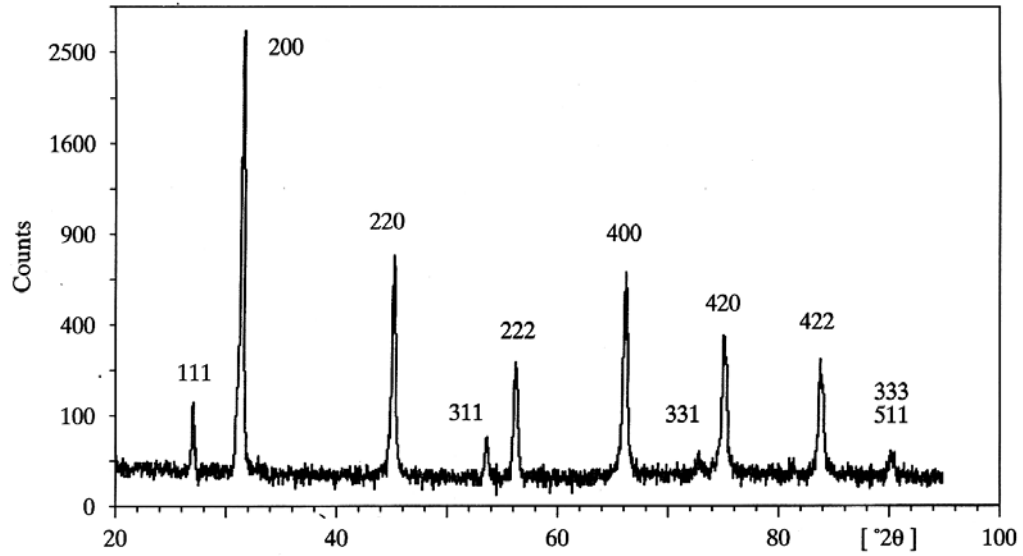


Figure 4.4: Example of x-ray diffraction pattern for sodium chloride powder [3].

The characteristic peaks correspond to specific phases and crystal orientations of the material and are indexed for a given diffraction angle using Bragg's law and the interplanar spacing equation of the crystal structure. The equations of plane spacing for α (hcp) and β (bcc) titanium phases are given below.

$$\alpha \text{ (hcp): } \quad \frac{1}{d^2} = \frac{4}{3} \left(\frac{h^2 + hk + k^2}{a^2} \right) + \frac{l^2}{c^2} \quad (4.6)$$

$$\beta \text{ (bcc): } \quad \frac{1}{d^2} = \frac{h^2 + k^2 + l^2}{a^2} \quad (4.7)$$

The (hkl) values represent the Miller indices of the crystal planes. The lattice constants are given by a and c [3].

Phase analysis was conducted with a Phillips X'Pert Pro MRD (Materials Research Diffractometer) using Cu-K α radiation ($\lambda = 1.5405 \text{ \AA}$). The characteristic peaks were identified, and the relative intensities of the crystal planes were compared.

4.2 Design of Experiments

Ti-6Al-4V PREP powder was used to build cylindrical test specimens in the Arcam A2 EBM machine. Tensile specimens were built according to ASTM E8 with a two-inch gage length. However, the samples were built slightly larger in the EBM machine in order to compensate for final machining of the parts. The specimens were built so that the growth direction was perpendicular to the tensile axis.

Four sets containing nine test samples in each were fabricated. Three of the sample sets underwent various heat treatments. The other set remained in the as processed condition for comparison. Heat treatments were performed well above the β transus temperature at 1030°C for varying times and cooling rates as described in Table 4.1. In order to avoid contamination problems, all heat treatments were done in an Abar industrial vacuum furnace, and argon gas was used for the air quench medium.

Table 4.1: Three post processing conditions applied to the EBM as-processed specimens.

	Temperature	Time	Cooling Rate
1	1030°C	1 hr	Air quenched 1.1°C/s
2	1030°C	1 hr	Furnace cooled 0.1°C/s
3	1030°C	2 hr	Furnace cooled 0.1°C/s

A CNC machine was used to remove the rough surface typical of the EBM process. One and a half millimeters were machined off each sample to provide a nice surface finish to eliminate any nucleation sites for cracks during tensile testing. The dimensions of the final machined part are given in Figure 4.5.

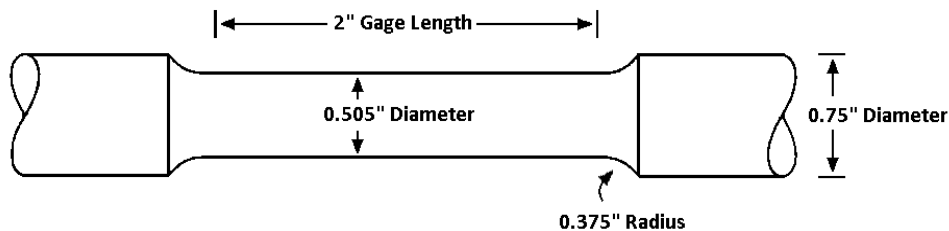


Figure 4.5: Dimensions of the final machined cylindrical tensile specimens built in the EBM machine.

Additional material at the ends of the tensile specimens were cut off and used for microscopy and x-ray diffraction analysis. The specimens were prepared for microscopy by mounting in a molding compound. Grinding and rough polishing were done with 60 to 1200 grit SiC. Fine polishing was performed on a microcloth using 1 micron alumina followed by 0.3 micron alumina. An ultrasonic cleaner was used before each polishing step and for final cleaning of the sample. The samples were etched for 15 seconds using Kroll's reagent (3mL HF, 5mL HNO₃, 100mL H₂O).

4.3 Referenced Literature

- [1] G. E. Dieter, Mechanical Behavior of Materials Under Tension, in: Metals Handbook, vol 8, ASM, Metals Park, 1985.
- [2] J. I. Goldstein, D. E. Newbury, P. Echlin, D. C. Joy, C. E. Lyman, E. Lifshin, L. Sawyer, J. R. Michael, Scanning Electron Microscopy and X-Ray Microanalysis, Springer, New York, 2003, p. 690.
- [3] B. D. Cullity, S. R. Stock, Elements of X-Ray Diffraction, Prentice Hall, Upper Saddle River, NJ, 2001, p. 664.

Chapter 5

Results and Analysis

5.1 Mechanical Properties

The mechanical properties were determined from the tensile tests performed under a constant motor extension rate of 0.2 in/min. Table 5.1 lists the averages of yield strength and tensile strength along with the percent elongation and reduction of area for each set of samples, including the as-processed and the three different heat treated specimens.

It is important to note that the elongation data is not truly representative since none of the samples broke within the extensometer gage. The samples were slightly tapered by as much as three-thousandths of an inch due to inaccuracy of the machining algorithm (Figure 5.1), therefore no samples failed at the center and instead broke at the narrowed end of the gage length. Even though the elongations are not conclusive, a relative comparison can be made between the as-processed and heat treated specimens. Because the samples broke at a location slightly smaller than the center, the yield and tensile strengths and the percent area in reduction values are misleading. Therefore, the values are recalculated using the average cross-sectional area of the narrowed end of the specimen and are listed in Table 5.2.

The tensile properties found in the current work are difficult to compare against earlier findings since different types of powder were used. Samples of previous work were prepared with gas-atomized powder whereas samples used in this study were built from PREP powder.

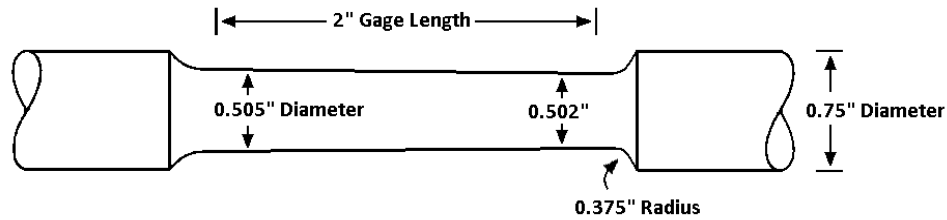


Figure 5.1: Schematic of the slightly tapered cylindrical tensile specimens after machining.

Comparing data in Table 5.2, the tensile and yield strengths of the electron beam melted process are similar to those provided by wrought and cast products. In the EBM as-processed condition, the strength was significantly higher than all other process conditions, however it is evident from the reduction in area that the ductility suffered. Some ductility is restored upon heat treatment. Of the four EBM process conditions, the specimens treated for one hour and air quenched provided the best reduction in area. Although the area reduction percentage does not meet the standard for wrought products, it does surpass the average value obtained for cast products.

The measured elongations of the EBM products cannot be compared to the wrought or cast conditions since fracture did not occur within the extensometer; however, a relative comparison of the EBM fabrication processes can be made. The two sets of β treated and furnace cooled specimens revealed no change in elongation compared to the EBM as-processed. Conversely, the β treated and air quenched specimens showed a two percent increase in elongation. Overall, the β treated and air quenched processing method of EBM Ti-6Al-4V provides the best combination of tensile properties.

Table 5.1: Mechanical properties of electron beam melted Ti-6Al-4V products evaluated using 0.0564 in² cross-sectional area and compared against wrought and cast products.

			UTS (MPa)	YS (MPa)	%EL	%RA
I	1	Electron beam melted	1092 (±6.9)	1047 (±12.5)	5* (±1.5)	13 (±4.7)
	2	β treated for 1 hr and air quenched	955 (±22.6)	870 (±20.5)	7* (±1.6)	23 (±2.6)
	3	β treated for 1 hr and furnace cooled	970 (±19.0)	866 (±22.9)	5* (±0.8)	18 (±2.6)
	4	β treated for 2 hr and furnace cooled	991 (±25.8)	871 (±22.5)	5* (±0.5)	17 (±4.3)
II		Cast bar, annealed [†]	1015	890	10	16
III		Wrought bar, annealed [†]	1000	925	16	34

* Fracture occurred outside of the extensometer gage.
[†] ASM Metals Handbook, 9th edition, Vol. 3

Table 5.2: Mechanical properties of electron beam melted Ti-6Al-4V products evaluated using 0.0539in² cross-sectional area and compared against wrought and cast products.

			UTS (MPa)	YS (MPa)	%EL	%RA
I	1	Electron beam melted	1143 (±7.2)	1095 (±13.1)	5* (±1.5)	9 (±4.9)
	2	β treated for 1 hr and air quenched	999 (±23.7)	911 (±21.5)	7* (±1.6)	20 (±2.7)
	3	β treated for 1 hr and furnace cooled	1015 (±19.9)	906 (±24.0)	5* (±0.8)	14 (±2.8)
	4	β treated for 2 hr and furnace cooled	991 (±25.8)	871 (±21.5)	5* (±0.5)	13 (±4.5)
II		Cast bar, annealed [†]	1015	890	10	16
III		Wrought bar, annealed [†]	1000	925	16	34

* Fracture occurred outside of the extensometer gage.
[†] ASM Metals Handbook, 9th edition, Vol. 3

5.2 Fractography

The fracture surfaces of the as-processed and heat treated tensile specimens were examined under an SEM for comparison. Low and high magnification images reveal different fracture modes between that of the as-processed and β heat treated samples.

The columnar grain structure, organized in a perpendicular fashion in Figures 5.2 and 5.3, is fairly distinguishable with tear ridges in the fractographs of the as-processed specimen. At higher magnification small equiaxed dimples are visible, which suggests ductile dimple rupture caused by microvoid coalescence (Figure 5.4). The equiaxed shape of the dimples indicates failure due to uniaxial tensile overload [1,2].

The columnar bands are not well defined in the fractographs of the heat treated specimens, and a much different fracture surface emerges as seen in Figures 5.5 and 5.6. This type of fracture appears to be a mixed mode of transgranular cleavage along the α (hcp) laths and dimple rupture with tear ridges at the grain boundaries. Also noted is the occurrence of intergranular cleavage cracking. (Intergranular fracture exists in the as-processed specimens too, but transpires by ductile dimple rupture and occurs less frequently). A higher magnification fractograph of the heat treated condition displays equiaxed and elongated dimples (Figure 5.7). The presence of both types of dimples implies more than one mode of fracture which includes pulling in tension in addition to shearing and/or tensile tearing. Glide plane decohesion steps, signifying plastic rupture, also are noticed in many regions of the heat treated specimens (Figure 5.8) [1,2].

A common feature which appeared in both the as-processed and heat treated fracture surfaces was fine dimples between the α (hcp) laths as a result of β (bcc) rupturing [1], which is illustrated in Figure 5.8.

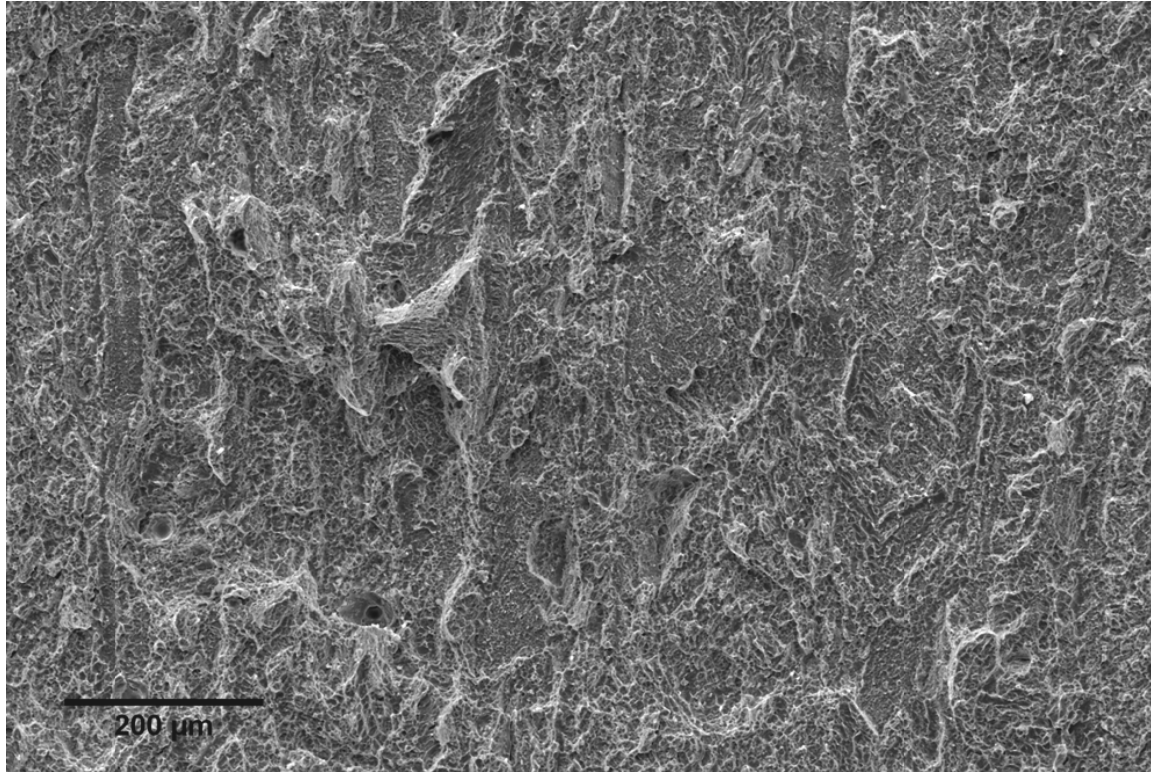


Figure 5.2: Fractograph of Ti-6Al-4V tensile specimen produced via EBM showing apparent columnar structure.

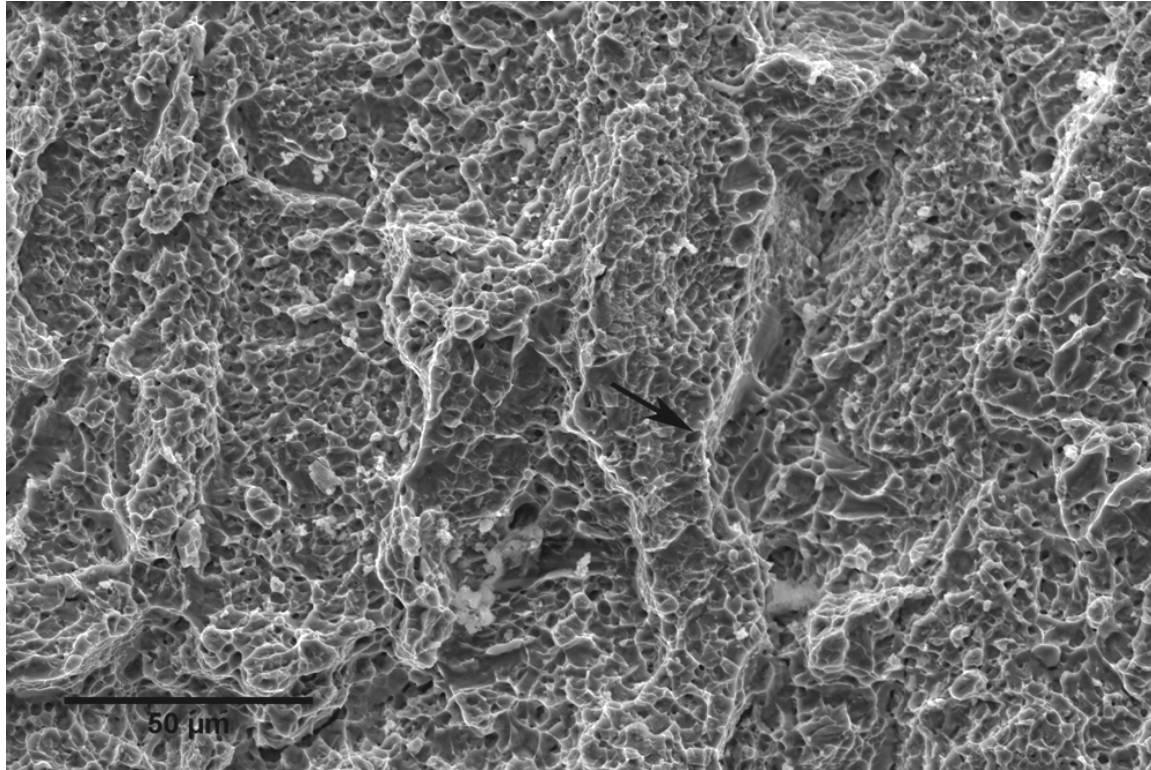


Figure 5.3: Fractograph of Ti-6Al-4V tensile specimen produced via EBM showing tear ridges (arrow) along apparent grain boundaries.

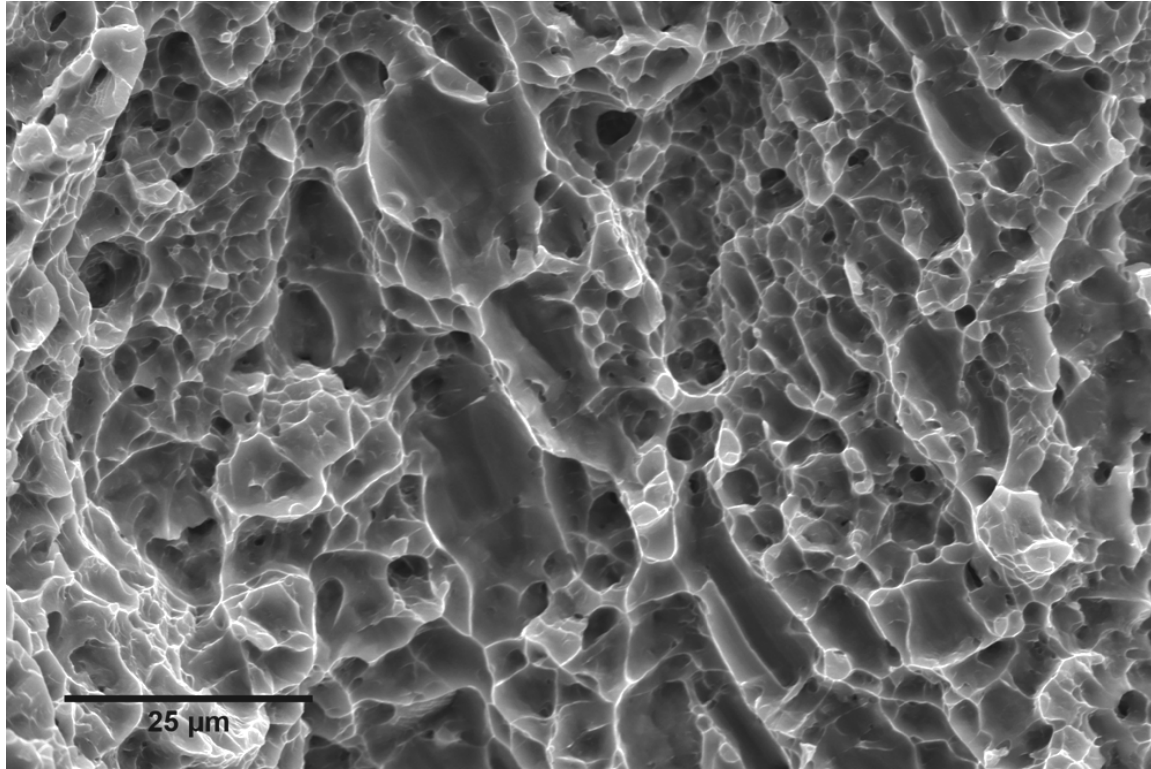


Figure 5.4: Fractograph of Ti-6Al-4V tensile specimen produced via EBM showing mostly small equiaxed dimples and several large dimples.

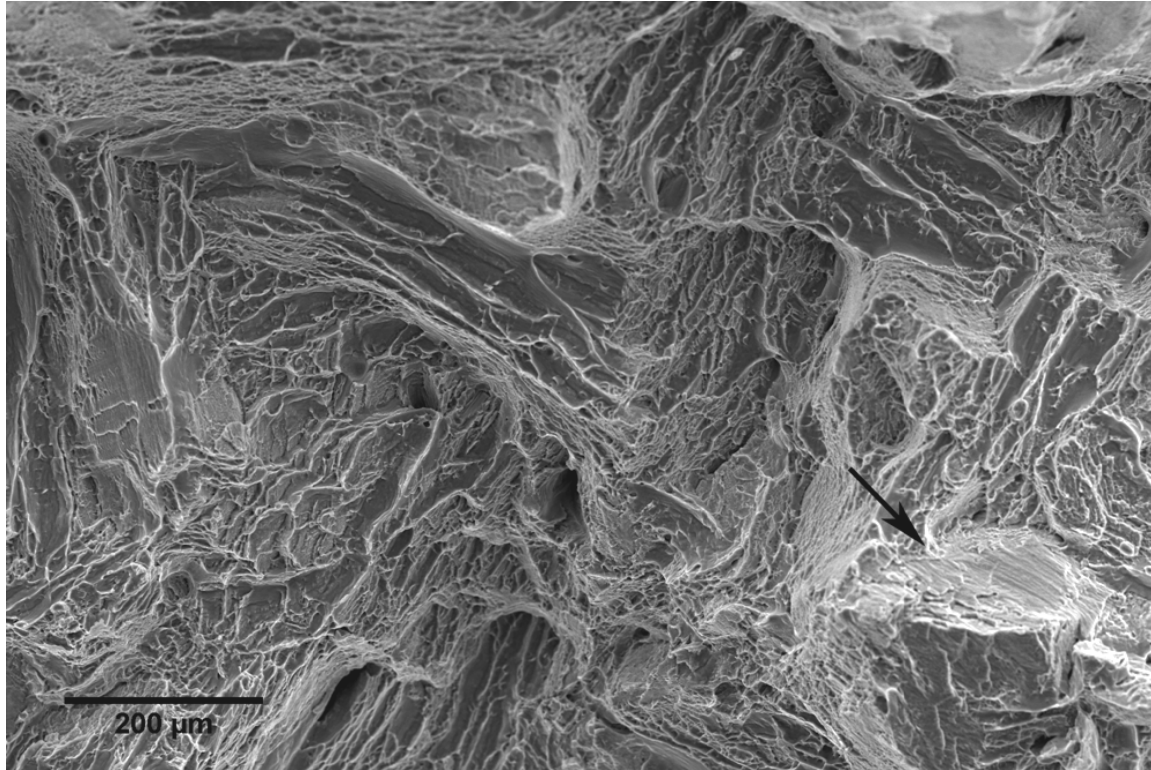


Figure 5.5: Fractograph of Ti-6Al-4V tensile specimen produced via EBM and β heat treated displaying a mixed mode of cleavage and dimple rupture. A cleavage fracture facet (arrow) is noted.

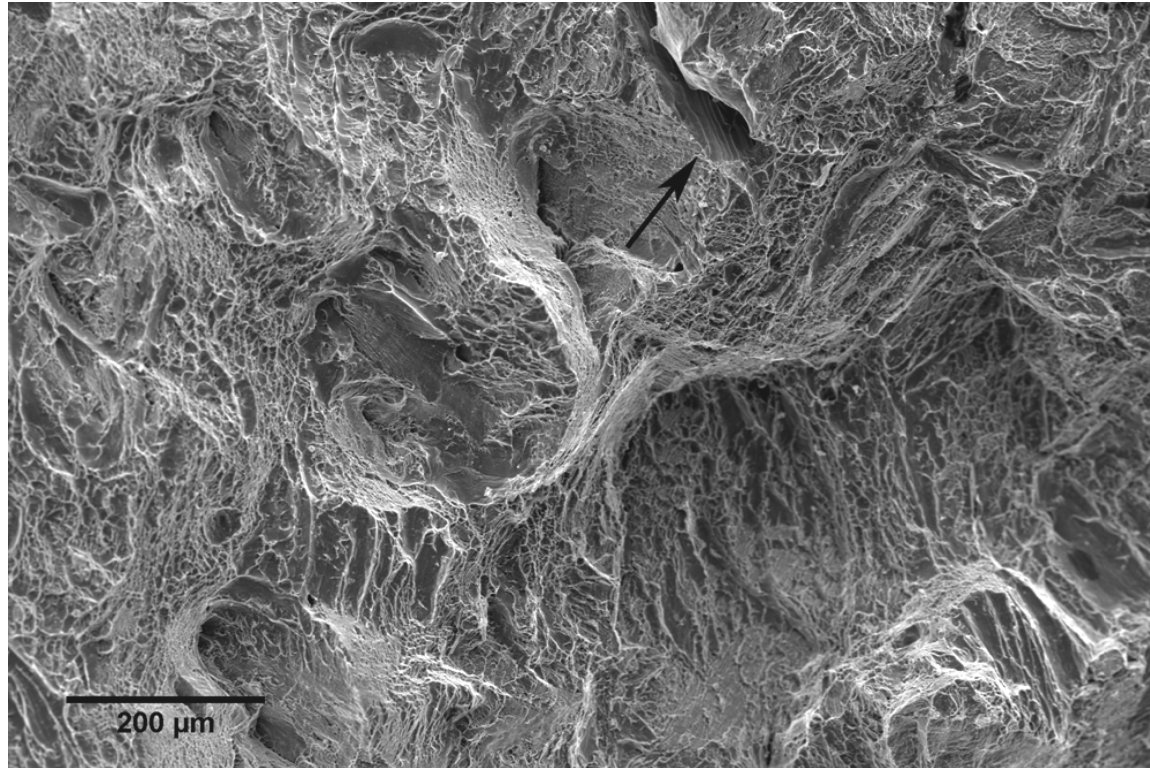


Figure 5.6: Fractograph of Ti-6Al-4V tensile specimen produced via EBM and β heat treated displaying a mixed mode of cleavage and dimple rupture. Intergranular fracture (arrow) is observed.

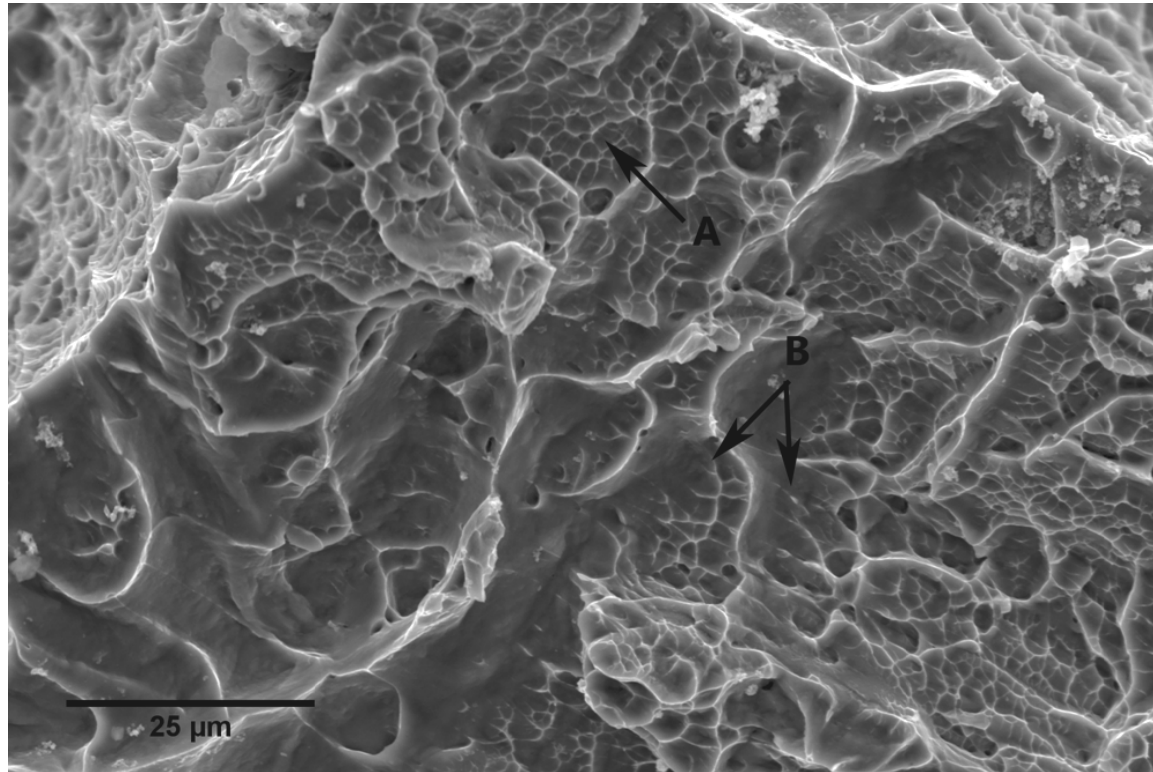


Figure 5.7: Fractograph of Ti-6Al-4V tensile specimen produced via EBM and β heat treated. Equiaxed and elongated dimples are indicated in regions A and B, respectively.

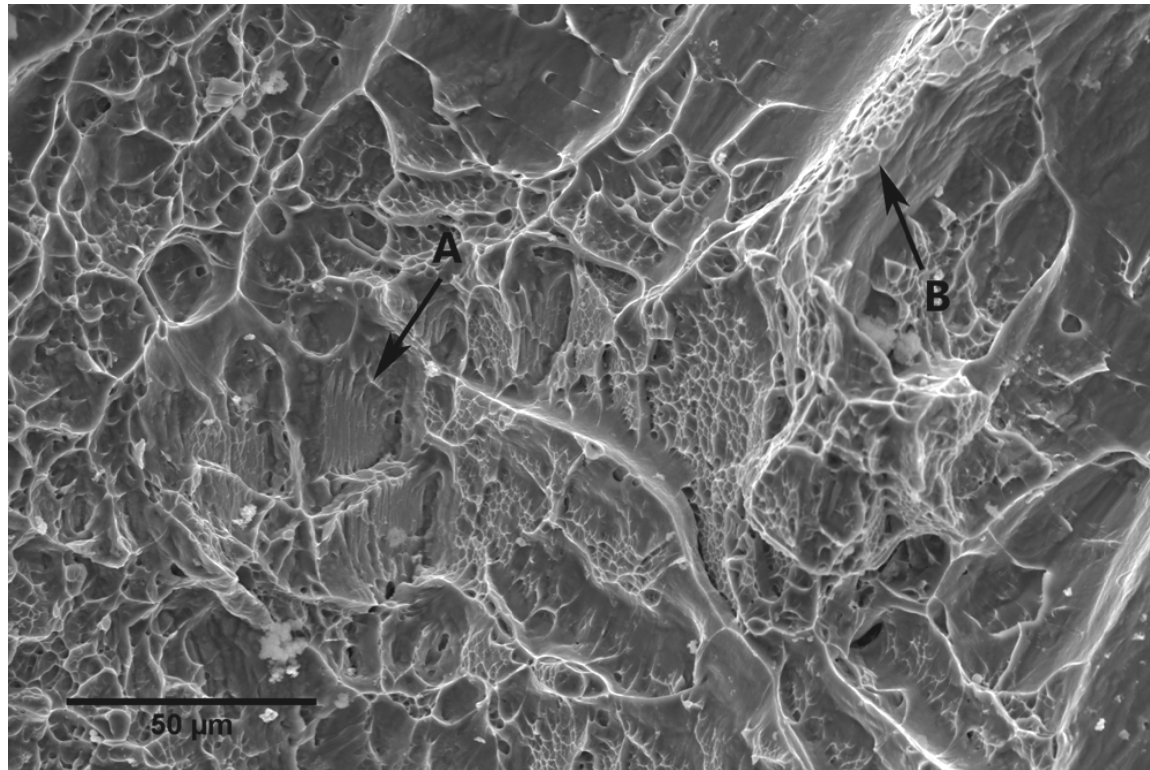


Figure 5.8: Fractograph of Ti-6Al-4V tensile specimen produced via EBM and β heat treated. Serpentine glide ridges are shown in region A, and small equiaxed dimples occur at the lath boundary in region B.

5.3 Microscopy

The microstructures of the EBM processes are analyzed to help explain the differences in the mechanical properties. As determined in previous research, the macrostructure of components produced from EBM consists of columnar grains which run parallel to the build direction. A macrostructure of equiaxed grains are observed at the cross-sectional ends of the columns. Figures 5.9 and 5.10, respectively, display the columnar and equiaxed structures observed in the EBM as-processed Ti-6Al-4V.

The microstructure of the as-processed EBM products consists of fine acicular α (hcp) and intergranular β (bcc) within α (hcp) grain boundaries. This type of microstructure is often referred to as a “basket weave” structure because the α (hcp) grains grow in preferred orientations which appear to be interlacing. The fine α (hcp) structure supports increased strength due to the small slip length path of the acicular microstructure thereby delaying crack nucleation [3-5].

Upon heat treating the EBM specimens above the β transus, the columnar macrostructure is less visible but does remain. It appears that equiaxed grains are formed thereby altering the columnar grain structure, as demonstrated in Figure 5.11, and a mixture of columnar and equiaxed grains occurs along the growth direction of the heat treated specimens. The equiaxed grains may have formed as a result of grain growth during heat treating in which areas of one columnar grain impinged upon the area of a neighboring grain creating a larger grain which was equiaxed.

A broad lamellar microstructure is formed after heat treating. Figure 5.12 represents the microstructure of the argon gas quenched specimens. The furnace cooled microstructures of the specimens heat treated for one hour and two hours are seen in Figures 5.13 and 5.14,

respectively. Common features for all the experimental heat treatments include coarse α (hcp) lamellae and blocky α (hcp), although the latter is more prevalent in the furnace cooled samples. Discontinuous and coarse α (hcp) also is seen at the grain boundaries in the micrographs of the heat treated samples. Large grain boundaries and blocky α (hcp) are crack initiation sites which lead to premature failure and short fatigue life [3,4,6,7]. The large, continuous α phase at the grain boundaries is perhaps the cause of the intergranular fracture noticed in Figure 5.6.

As mentioned in a previous section, the tensile and yield strengths of the heat treated specimens are lower than that of the as-processed EBM. This is likely an effect of the grain boundary coarsening and the broad lamellar microstructure. The reduction in area, however, improves after heat treating and is most noticeable for the air quench condition. The reason for better ductile properties in the argon gas quenched samples compared to the other tested heat treatments is possibly because there is a smaller amount of large, blocky α (hcp) as well as a colony microstructure in which the α (hcp) forms on several invariant planes. The existing colony microstructure assists in retarding crack propagation as it creates a tortuous path for cracks [3-6].

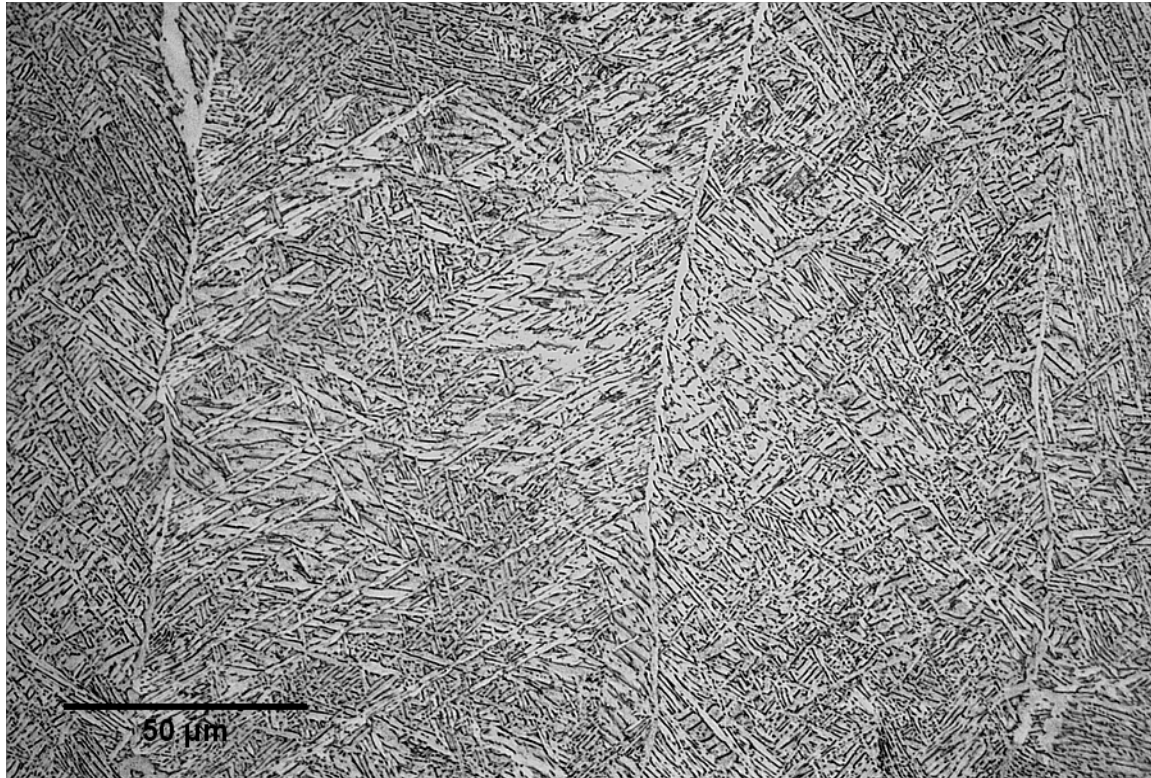


Figure 5.9: Optical micrograph of Ti-6Al-4V produced via EBM showing the columnar structure parallel to the build direction.

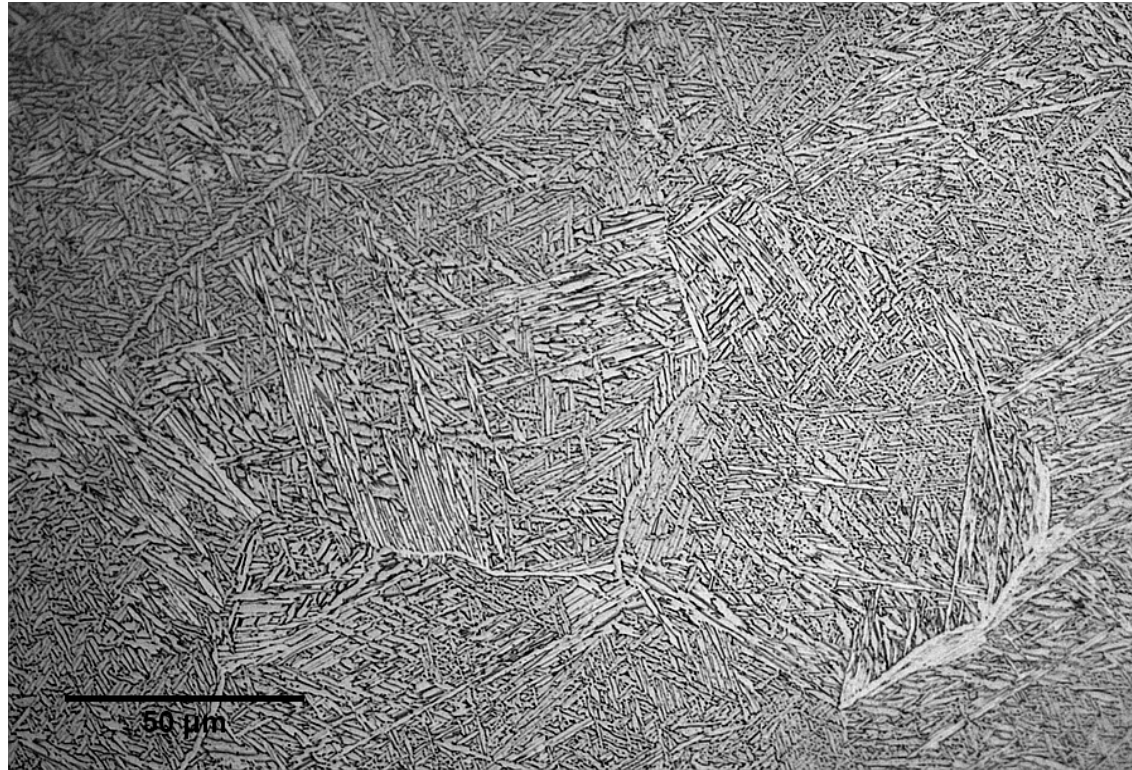


Figure 5.10: Optical micrograph of Ti-6Al-4V produced via EBM showing the equiaxed structure at the cross-sectional ends of the columnar structure.

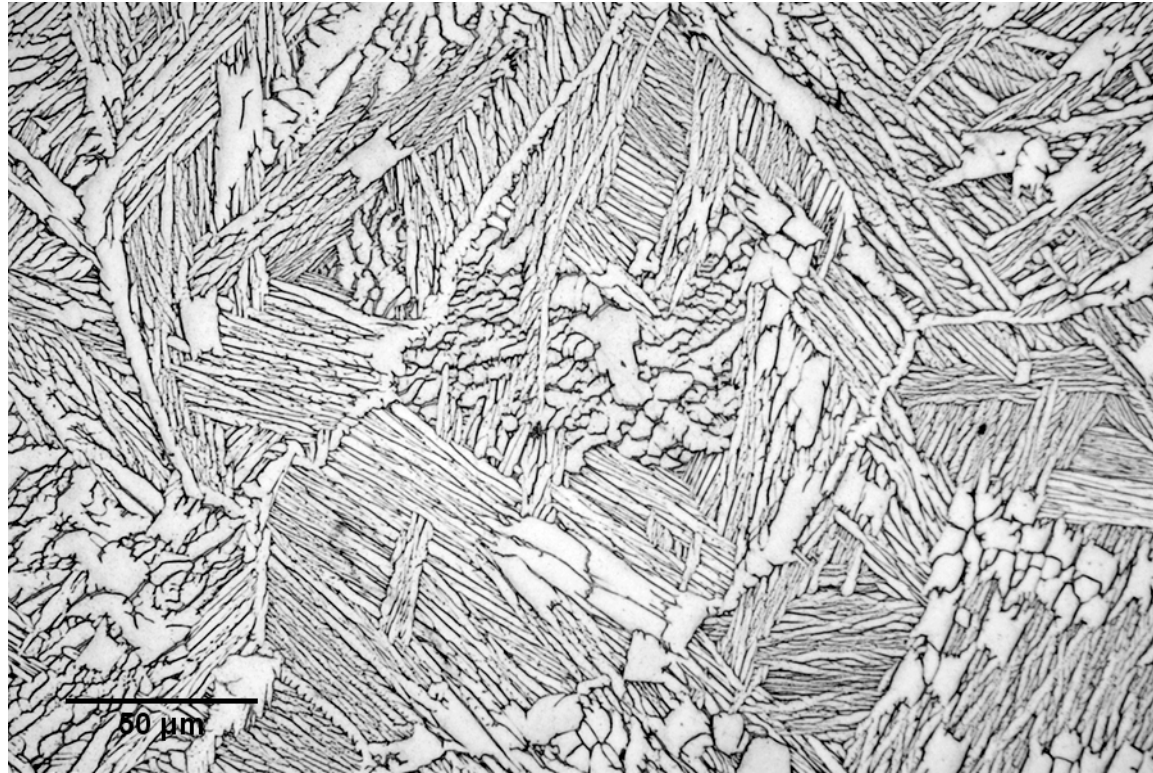


Figure 5.11: Optical micrograph of Ti-6Al-4V produced via EBM which has been β treated showing an equiaxed grain along the growth direction.

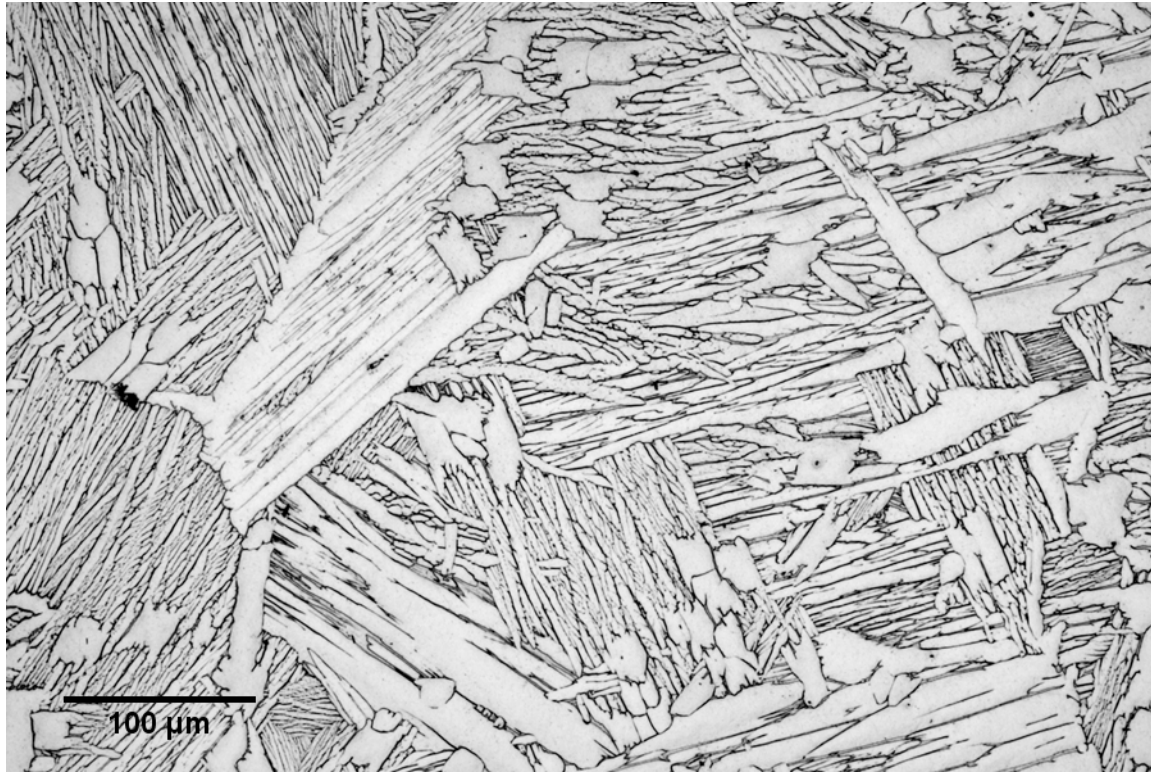


Figure 5.12: Optical micrograph of Ti-6Al-4V produced via EBM and β treated for one hour and argon gas quenched

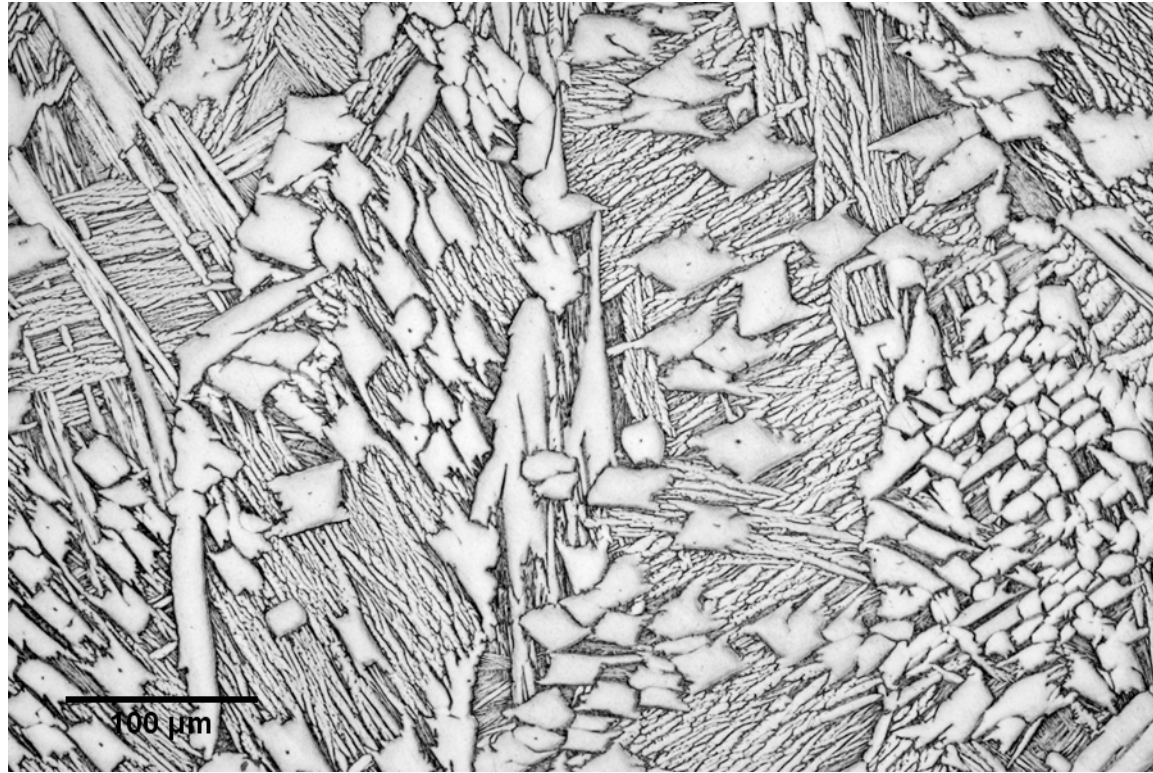


Figure 5.13: Optical micrograph of Ti-6Al-4V produced via EBM and β treated for one hour and furnace cooled.

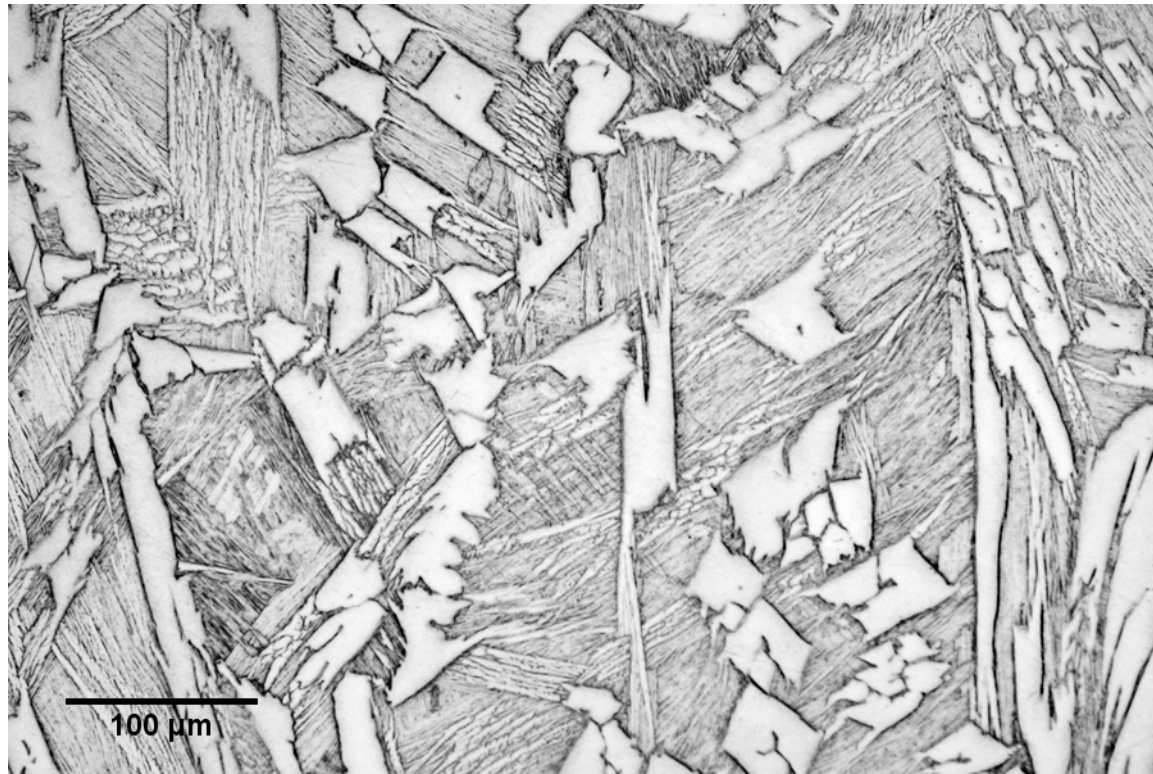


Figure 5.14: Optical micrograph of Ti-6Al-4V produced via EBM and β treated for two hours and furnace cooled.

5.4 Phase Analysis

X-ray diffraction was performed for each set of experimental conditions to compare the relative amounts of phases present. PeakFit software was used for analysis of the diffraction curve, and a Gaussian distribution of the peaks was assumed for identifying all possible peaks. Established by Bragg's law and the crystal structure, a total of ten possible reflections can occur in the 2θ range tested, seven of which belong to the α (hcp) phase, and the remaining three are the β (bcc) phase. Table 5.3 gives the calculated diffraction angles of the possible crystallographic plane reflections for α (hcp) and β (bcc) phases. The positions of the peaks were determined using the lattice parameters for pure titanium ($a = 2.9512 \text{ \AA}$, $c = 4.6845 \text{ \AA}$ for α -Ti and $a = 3.3066 \text{ \AA}$ for β -Ti) [8]. The peak positions may be slightly shifted from the calculated values in the x-ray diffraction patterns of the Ti-6Al-4V alloy.

All possible peaks can be seen in the as-processed EBM process in Figure 5.15. The α (hcp) peaks align with the estimated diffraction angles, however the β (bcc) peaks are slightly shifted from the calculated. The calculated and measured diffraction angles of each reflection plane are compared in Table 5.4. Using Bragg's law (Equation 4.5) and the equation of plane spacing for β (bcc) titanium phase (Equation 4.7), the actual lattice parameter of β (bcc) in Ti-6Al-4V is 3.2230 \AA at room temperature, established from the measured data. Therefore, the retained β contracts by as much as 0.0836 \AA upon cooling to room temperature in the Ti-6Al-4V alloy.

Heat treating the samples alters the degree of texture seen by comparing the as-processed EBM spectrum to the following heat treated spectra (Figures 5.16, 5.17, and 5.18). All of the x-ray diffraction patterns acquired for the heat treated specimens show an apparent change in the intensity of the hcp (101) crystal plane with respect to the other phase orientations within a given spectrum. The relative intensity of this orientation increases in the spectra of the heat

treated samples which suggests preferential growth of this orientation after heat treating in the β region. The favorable rearrangement of slip systems due to the change in α lath orientation is a plausible cause for the improvement of ductility found in all the heat treated specimens when the tensile load is applied perpendicular to the columnar grain structure. Further testing is needed to determine how this affects tensile specimens with the tensile load applied parallel to the columnar structure.

Table 5.3: Calculated 2θ values for possible reflections in the measured range.

α (hcp)				β (bcc)			
	hkl	d (Å)	$2\theta^\circ$		hkl	d (Å)	$2\theta^\circ$
1	(002)	2.34	38.4	1	(200)	1.65	55.6
2	(110)	1.48	63.0	2	(110)	2.34	38.5
3	(101)	2.24	40.2	3	(211)	1.35	69.7
4	(200)	1.28	74.2				
5	(100)	2.56	35.11				
6	(102)	1.73	53.0				
7	(103)	1.33	70.7				
a = 2.9512 Å c = 4.6845 Å				a = 3.3066 Å			

Table 5.4: Comparison of calculated and measured diffraction angles.

α (hcp)				β (bcc)			
	hkl	$2\theta^\circ$			hkl	$2\theta^\circ$	
		Calculated	Measured			Calculated	Measured
1	(002)	38.4	38.4	1	(200)	55.6	57.3
2	(110)	63.0	63.3	2	(110)	38.5	39.4
3	(101)	40.2	40.3	3	(211)	69.7	71.7
4	(200)	74.2	74.4				
5	(100)	35.1	35.2				
6	(102)	53.0	53.1				
7	(103)	70.7	70.8				
a = 2.9512 Å c = 4.6845 Å				a = 3.3066 Å			

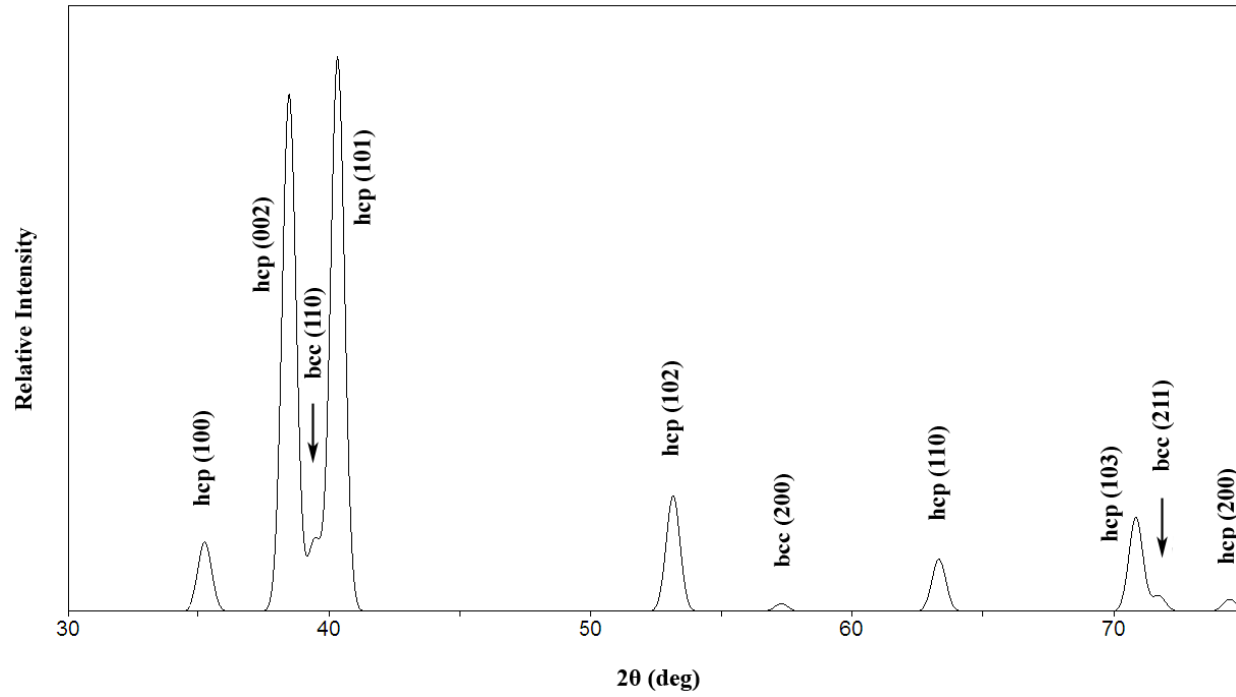


Figure 5.15: X-ray diffraction pattern of Ti-6Al-4V produced via electron beam melting process.

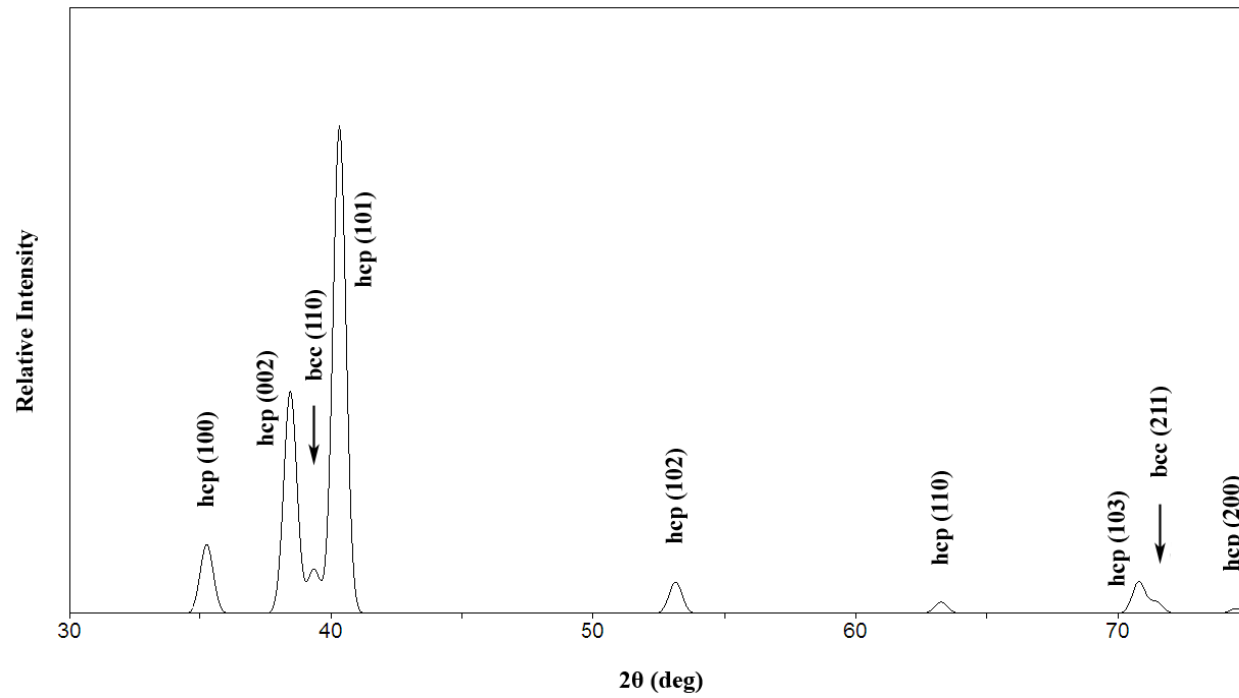


Figure 5.16: X-ray diffraction pattern of Ti-6Al-4V produced via EBM and β treated for one hour and argon gas quenched.

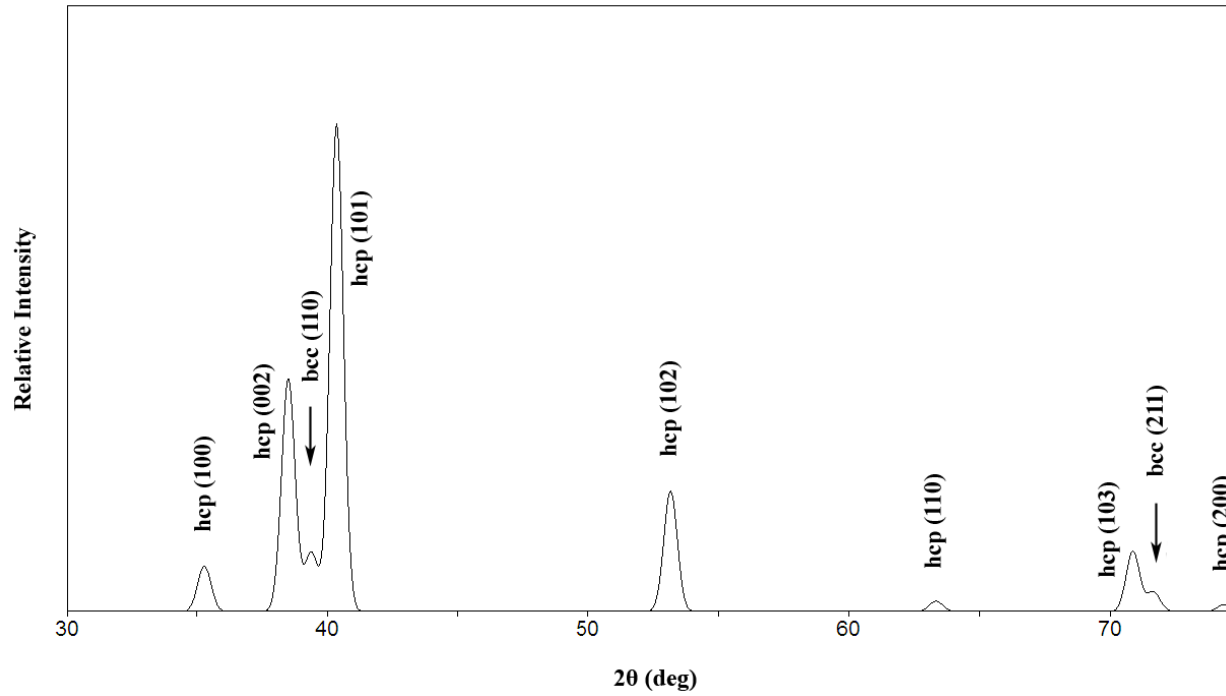


Figure 5.17: X-ray diffraction pattern of Ti-6Al-4V produced via EBM and β treated for one hour and furnace cooled.

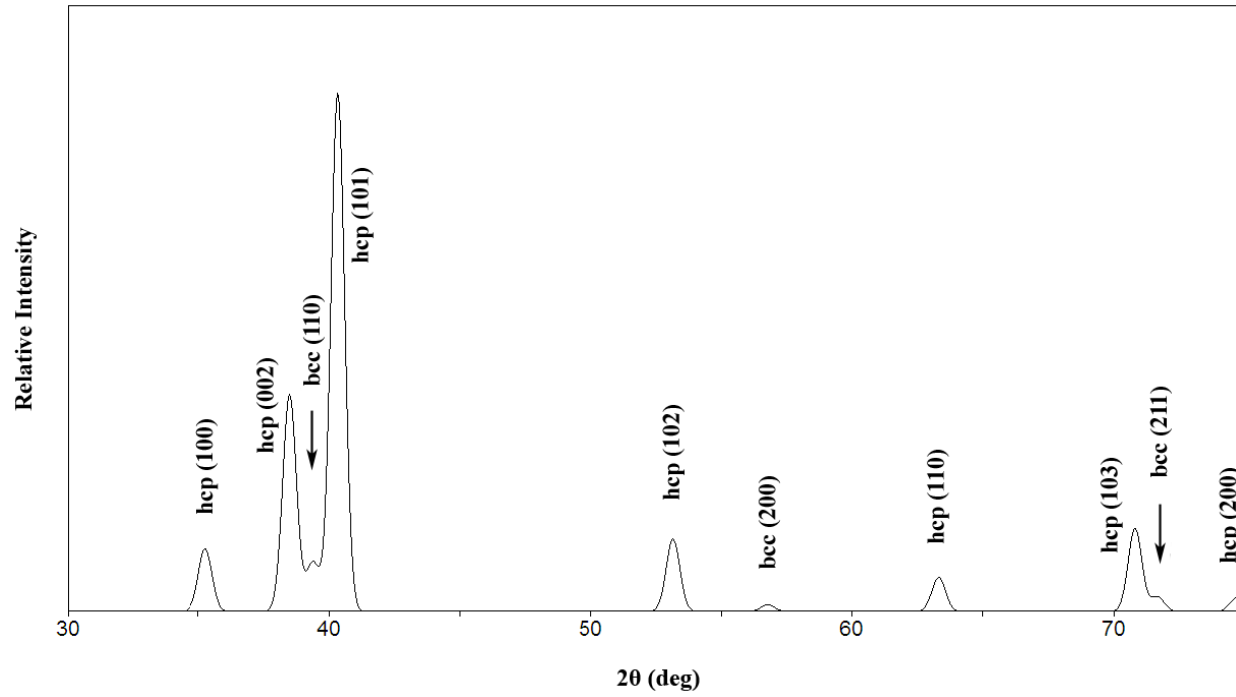


Figure 5.18: X-ray diffraction pattern of Ti-6Al-4V produced via EBM and β treated for two hours and furnace cooled.

5.5 Referenced Literature

- [1] V. A. Joshi, Titanium Alloys: An Atlas of Structures and Fracture Features, Taylor & Francis, Boca Raton, 2006, p. 227.
- [2] V. Kerlins, Modes of Fracture, in: Metals Handbook, vol 12, ASM, Metals Park, 1985, pp. 12-71.
- [3] J. Matthew J. Donachie (Ed.) Titanium: A Technical Guide, ASM, Metals Park, 2000, p. 381.
- [4] C. Leyens, M. Peters (Eds.), Titanium and Titanium Alloys: Fundamentals and Applications, Wiley, Weinheim, 2003, p. 532.
- [5] R. Filip, K. Kubiak, W. Ziaja, J. Sieniawski, Journal of Materials Processing Technology 133 (2003) 84-89.
- [6] J. C. Williams, Titanium alloys: production, behavior and application, in: H. M. Flower (Ed.) High Performance Materials in Aerospace, Chapman & Hall, Cambridge, 1995, pp. 85-134.
- [7] W. F. Smith, Titanium and Its Alloys, in: Structure and Properties of Engineering Alloys, McGraw-Hill, New York, 1993, p. 630.

Chapter 6

Conclusions

6.1 Summary

- For all β treated conditions, the ductility increased compared to the as-processed EBM specimens. The greatest ductility is found in the samples treated in the β region for one hour and argon gas quenched.
- Ductile dimple fracture seen in the as-processed condition changes to transgranular cleavage with ductile dimple rupture along the α laths for all heat treatments.
- The microstructure contrasted greatly between the as-processed and heat treated specimens. After heat treating above the β transus, the columnar structure is less obvious but does occur. A mixed columnar and equiaxed structure is apparent.
- One possible reason for better ductile properties in the heat treated EBM specimens is the presence of a colony microstructure formed upon cooling from the β region. The colony microstructure assists in retarding crack propagation as it creates a tortuous path for cracks.
- The favorable rearrangement of slip systems due to the change in α lath orientation also may have contributed to the improvement of ductility.

6.2 Future Work

- All tensile testing was performed perpendicular to the EBM growth direction. Further testing with the tensile load applied parallel to the growth direction is required to determine if the increase in ductility from β heat treating occurs along both tensile axes. Quantitative texture analysis using pole figures should be investigated to determine the orientation effects on the deformation behavior for both test directions.
- Blocky α and grain boundary coarsening may be minimized by using shorter heating times and/or lower temperatures during heat treatment. On the other hand, longer heating times and slower cooling rates may allow the blocky α to spheroidize creating equiaxed α grains which enhance ductility. Hence, new heat treatment regimes may be considered to test the effects they have on the tensile properties.
- Future work also should include the addition of trace amounts of boron to the alloy. Significant grain refinement was found in as-cast Ti-6Al-4V when between 0.1 and 1 weight percent of boron was added to the alloy. The grain refinement is thought to be due to solute partitioning between the β phase and the boron which leads to constitutional supercooling ahead of the solidification front. A combination of the temperature difference at the liquid/solid interface and the presence of boron promote nuclei formation [1]. Furthermore, equiaxed α has been observed from subsequent heat treatment by slowly cooling from the β region in Ti-6Al-4V-2B alloy. TiB likely promotes additional nucleation sites from which α may grow [2].
- Ultrasonic vibration during processing has proven to reduce the grain size for other alloys in several studies. The vibratory response is a result of fragmentation of the crystals during growth [3]. The application of ultrasonic vibration during the EBM process may enhance grain refinement and thus the mechanical properties.

6.3 Referenced Literature

- [1] S. Tamirisakandala, R. B. Bhat, J. S. Tiley, D. B. Miracle, *Scripta Materialia* 53 (2005) 1421-1426.
- [2] D. Hill, R. Banerjee, D. Huber, J. Tiley, H. L. Fraser, *Scripta Materialia* 52 (2005) 387-392.
- [3] L. Nastac, M. N. Gungor, I. Ucok, K. L. Klug, W. T. Tack, *International Journal of Cast Metals Research* 19 (2006) 73-93.